A *Plasmodium falciparum* redox survival mechanism licenses killing by artemisinins

Smritikana Dutta[1], Mohammad Faaiz[1], Saikat Bhattacharjee[2], Kasturi Haldar[3,*] and Souvik Bhattacharjee[1,*]

[1] Special Centre for Molecular Medicine, Jawaharlal Nehru University, New Delhi 110067. India.

[2] Regional Center for Biotechnology, 3rd Milestone, Faridabad-Gurgaon Expressway, Faridabad, Haryana 121001. India.

[3] Department of Biological Sciences, University of Notre Dame, Notre Dame, Indiana, IN 46556, USA.

[*] Corresponding authors

Corresponding authors address:

souvik@jnu.ac.in . Special Centre for Molecular Medicine, Jawaharlal Nehru University, New Delhi 110067. India.

khaldar@nd.edu. Department of Biological Sciences, University of Notre Dame, Notre Dame, Indiana, IN 46556, USA.

Abstract

Mutations in *Plasmodium falciparum* Kelch13 (K13) confer artemisinin resistance (ART-R) which threatens global malaria control, but known K13 functions fail to explain clinical ART-R. We reported that K13 binds the oxidant heme *in vitro*, however, its functions in redox-stress, cell survival and death remained unknown. Since taut control of free heme is not feasible in infected erythrocytes, we utilized a non-erythroid cell model to show that K13 directly binds and is stabilized by nanomolar heme levels. K13 also binds and regulates a major redox transcription factor, which is displaced by heme into the nucleus, to raise redox-stress responses that become suppressed during artemisinin-induced death (ART-death). K13's evolutionarily conserved kelch domain confers heme-binding and ART-death characteristics to its mammalian orthologue KEAP1. Chemical or genetic elevation of K13, fuels ART-death proportionate to K13 levels even in vast excess of heme, suggesting a novel plasmodial redox-survival mechanism licenses ART-death in clinical ART-R.

31 **Introduction**

32 Artemisinins (ARTs) are highly effective in curing blood-stage infection of *Plasmodium falciparum,* the
33 deadliest of human malaria parasites[1]. These drugs are critical components of artemisinin-based
34 combination therapies (ACT) that have played a key role in reducing the global burden of malaria and
35 remain the cornerstone of its control worldwide[2]. Despite the prevalent model that ART kills through
36 indiscriminate alkylation and damage of parasite lipids, proteins and DNA[3–5], robust clinical resistance
37 has been ascribed to one major gene *Pfkelch13* (K13; PlasmoDB ID: PF3D7_1343700)[6], which has
38 been shown to be causal for resistance[7]. Since ART-resistance (ART-R) poses a significant threat to
39 malaria control[8,9], K13 has been intensely studied over the last decade[10–14]. The consensus data
40 suggest that it possess an evolutionarily conserved 'kelch domain' is cytoplasmically synthesized and
41 associated with vesicular structures, including the parasite's digestive endosomes, apicoplast,
42 mitochondria, endoplasmic reticulum as well as vesicles enriched in Rabs, ATG18 and
43 phosphatidylinositol 3-phosphate (PI3P)[9–11]. At the parasite's trophozoite stage, when haemoglobin
44 uptake and digestion are most active, K13 regulates endocytosis *via* structures called cytostomes,
45 and resistance mutations suppress this process[15,16]. But notably, these very trophozoite stages
46 harbouring K13 resistance mutations remain highly susceptible to ART suggesting that while
47 hemoglobin uptake regulated by K13, it may not be the major target of resistance, which may arise
48 from changes in additional but still unknown functions of K13.

49 ARTs are 'pro-drugs' in that they must all be converted to dihydroartemisinin (DHA) and which in turn
50 is subsequently activated to release their killing action. High (micromolar) concentration of heme
51 have been shown to increase ART-potency because it cleaves the endoperoxide bridge yielding
52 highly reactive oxy-centered and C4-centered radicals[17] that alkylates a wide range of cellular
53 components causing oxidative damage, which results in parasite cell death[18,19]. Malaria parasites
54 digestion of host hemoglobin actively produces heme in the parasite's food vacuole (FV). Heme is
55 presumed to confer the sensitivity of ARTs in killing malaria parasites[20,21]. However, it is poorly
56 understood whether this can be achieved by physiological heme concentrations and how killing is
57 effected in 'ring' parasites early in blood-stage infection that lack a food vacuole, yet are critical
58 clinical targets of ART-R[22,23].

59 We have recently reported that recombinant and parasite-derived K13 directly bind molecular heme
60 with a dissociation constant (K_d) of 61.5 nM[24]. Heme binds to many proteins[25,26]. This includes
61 albumins with a K_d range of 2-40 μM[27], explaining their ready capacity to transfer heme to wide range
62 of acceptors[28]. In contrast heme-oxygenases which degrade heme, bind it with nanomolar (3-300
63 nM) affinity[29]. This suggests that with a K_d of 61.5 nM, K13 engages in at least moderately tight heme-
64 binding. Heme binding is known to effect profound structural changes in proteins[30] and heme is
65 implicated in oxidative stress metabolism[31]. However, the consequences of heme binding for K13's
66 stability and turnover, and whether heme-binding induces K13-mediated redox-controlled responses
67 remain entirely unknown. Furthermore, K13's engagement of antioxidant and detoxification systems,
68 as regulated by its closest mammalian orthologue Kelch-like ECH-associated protein 1 (KEAP1)[6,32,33]
69 has not been investigated. Finally, the implications of dislodging or neutralizing heme bound to K13,
70 for mechanisms of ART-based killing remain to be discovered.

71 Since *in vitro* studies suggest that K13 binds heme with a K_d of 61.5 nM[24], regulation of associated
72 cellular mechanisms may be expected to be initiated at nanomolar to low micromolar concentrations.
73 However, carefully controlling heme levels in this range remains unfeasible in blood-stage parasites.
74 This is because the host erythrocyte contains high levels of hemoglobin (3.2-3.6 mM)[34], whose
75 digestion is a major source of parasite heme. Erythrocytes also contain high levels (21 ± 2 μM) of free
76 heme[35] which may translocate through passive and facilitated pathways[26,36]. Since mature human red
77 cells are enucleated and terminally differentiated, these host sources of heme cannot be genetically
78 'turned off' post infection. Moreover, their reduction compromises parasite health[37]. Genetic or
79 chemical targeting of parasite's *de novo* heme biosynthesis in infected erythrocytes appears to have
80 no effect on parasite growth[38,39], suggesting that heme provided by exogenous pathways can be
81 supplemented from host-derived sources. Notably, free heme levels in most non-erythroid cells are in
82 the nanomolar range (25-300 nM)[36], but in *P. falciparum* they are reported to be considerably higher
83 (at 1.6 μM or more)[40,41], suggesting that throughout blood-stage infection the parasite may reside in a
84 high intracellular heme-rich environment, but the consequences for redox stress remain obscure.

85 We desired a cell system to study the molecular functions of K13 and their regulations by nanomolar
86 concentrations of heme. We therefore used a model non-erythroid mammalian cell line Du145[42] with
87 reduced levels of KEAP1, adapted to grow in heme-depleted media, and whose free heme levels

88 were tightly regulable by blocking endogenous heme biosynthetic enzymes. These Du145 cells were
89 otherwise capable of an active redox response[43]. Our goal was to query whether K13 and/or heme
90 contribute to redox-stress responses well as obtain mechanistic understanding of how either or both
91 trigger sensitization of cells to killing by ARTs and validate the model system as a rapid, functional
92 screen to identify redox cell survival and death mechanisms of *Plasmodium falciparum* malaria

93 **Results**

94 **K13 cellular levels are increased by heme-binding and -stabilization**

95 Human Du145 cells (HTB-81, ATCC, *www.atcc.org*) contain a full length wild-type *Keap1* gene, but
96 CpG dinucleotide methylation of its core promoter results in low *keap1* mRNA expression[44], making
97 them suitable for ectopically expressing kelch domain proteins with minimal interference from the
98 native KEAP1 protein. Sequence comparison clearly revealed that K13 is a homologue of KEAP1
99 (**Supplementary Fig. 1a**). We generated three stable transgenic lines expressing: (i) K13 as a C-
100 terminus fusion to GFP; K13-GFP, (ii) GFP alone, as well as (iii) a C-terminus fusion of flag-strep tag
101 KEAP1 (see *Materials and Methods*). Indirect immunofluorescence assays (IFA) with quantitative
102 analyses, suggested cellular distribution of K13-GFP, GFP and KEAP1, at comparable levels in
103 transgenic Du145 cells (**Supplementary Fig. 1b)**. K13-GFP, GFP and flag-strep tag KEAP1
104 respectively appeared as fusion proteins at expected sizes of 105-kDa, 27-kDa and 80-kDa
105 (**Supplementary Fig. 1c, d**).

106 We recently showed that *in vitro* heme bound recombinant K13 protein (TrK13-WT) with high
107 affinity[24], but action of heme in cells was not known. Since the K_d for heme binding to K13 protein was
108 61.5 nM, we wanted to measure the effects at low nanomolar concentrations of heme. This required
109 growing Du145 cells under conditions where available heme was substantially depleted from the
110 extracellular sources, and the production of biosynthetic heme was blocked by inhibitors. Fetal bovine
111 serum (FBS) is the largest extracellular donor of heme and contributed median concentration of 3.2 ±
112 0.06 μM heme to culture media. We reduced FBS concentrations of heme to <850 nM
113 (**Supplementary Fig. 2a, b**) to create heme-depleted media (HDM; *Material and Methods*). Since the
114 K_d of heme for albumins is >1 μM, this was expected to dramatically reduce the transfer of
115 extracellular heme to cells. We also added succinylacetone [SA; an inhibitor of the second enzyme of

116 heme biosynthesis pathway, δ-aminolevulinic acid (ALA) dehydratase] to the culture media, which
117 restricted intracellular *de novo* heme synthesis. Our overall goal was to achieve culture conditions that
118 would be responsive to nanomolar concentrations of exogenously added heme. Accordingly, under
119 HDM conditions, the parental Du145, transgenic GFP and K13-GFP cells all showed intracellular
120 concentrations of ~60 nM heme. Addition of extracellular heme at 5 μM, raised intracellular heme to
121 400-450 nM. When extracellular concentrations were raised to 50 μM, the intracellular levels
122 plateaued at ~750 nM (**Supplementary Fig. 2c**). Together these data suggested that in the course of
123 all experiments intracellular heme concentrations ranged from ~60-750 nM.

124 K13-GFP cells cultured in HDM (K13-GFP^{HDM}) were subsequently exposed to different concentrations
125 of exogenously added heme (0-5 μM) in the media (referred to as heme-replenished media). As
126 shown in **Fig. 1a**, concentrations of 10 nM heme induced detectable increase in K13-GFP levels.
127 Progressive increase of K13-GFP levels were seen at 50 nM, 100 nM, 1 μM and 5 μM heme. At 5 μM
128 heme, K13-GFP levels were restored to those seen in K13-GFP 'control' cultures (**Fig. 1b**). There was
129 no effect on the cellular viability of K13-GFP (or GFP) expressing cells at 5 μM heme;
130 (**Supplementary Fig. 2d:** the IC_{50} for heme was ~25-fold higher for all cells). Notably, there was no
131 detectable change in the relative intensity of GFP or KEAP1 proteins when cells were subjected to
132 heme depletion or when supplemented with 5 μM heme (**Supplementary Fig. 2e, f**).

133 We next investigated the specificity of heme action. As shown in **Fig. 1c,** PPIX alone or when
134 complexed with Zn, had no effect even at 50 μM. However, increasing heme levels from 5 to 50 μM
135 continued to steadily increase levels of K13-GFP. Together, the data suggest that heme at
136 extracellular concentrations of 10 nanomolar or higher (and up to 50 μM) increase cellular levels of
137 K13-GFP (but not GFP or KEAP1), suggesting it is specific for K13. Increases in K13 were only
138 mediated by heme (not PPIX or Zn-PPIX) and likely due to heme's directly binding to K13 (since we
139 have previously shown that heme binds K13 with nanomolar affinity *in vitro*[24]).

140 Amongst heme binding proteins, hemopexin, a serum glycoprotein (which displays highest affinity for
141 heme at K_d ~ 1 pM[45,46]) has been reported to show heme-dependent resistance to protease
142 digestion[45]. We therefore investigated if the protease sensitivity of K13 was altered in its heme-bound
143 state. For *in vitro* assay, we used the affinity purified 61-kDa recombinant TrK13-WT protein as K13
144 representative, described in our previous studies[24,47]. Recombinant TrK13-WT protein (10 μM) was

145 incubated with or without equimolar concentrations of heme and desalted to remove excess unbound
146 heme (see *Materials and methods*). Heme-bound TrK13-WT protein was subsequently treated with
147 trypsin under optimal buffer and pH conditions for varied incubation times. For trypsin (a serine
148 protease that cleaves between the carboxyl group of arginine or lysine and the amino group of the
149 adjacent amino acid), we also included commercially procured BSA, a confirmed heme-binding
150 protein[48] (but with substantially lower affinity) as a control. As shown in **Fig. 1d**, Coomassie-stained
151 SDS-PAGE revealed full-length (FL) TrK13-WT protein at 61-kDa. Treatment with trypsin yielded
152 additional low molecular weight fragments (doublets at 30-kDa and at 12-kDa; blue arrowheads) in
153 the absence of heme, whose appearance was blocked when the TrK13-WT protein was pre-
154 incubated with heme. Heme-binding only conferred partial resistance of BSA to trypsin
155 (**Supplementary Fig. 2g**). In absence of heme, multiple small protein fragments were detected (from
156 22-40 kDa; green arrowheads), while in its presence, larger fragments were observed at 45-55-kDa
157 (red arrowheads). The effects of heme on trypsin digestion of both TrK13-WT protein and BSA were
158 likely because of changes in the 3-dimensional conformation of these proteins (which is consistent
159 with previous reports in the literature[48] and observed in our earlier CD studies[24]). As shown in **Fig. 1e**,
160 resistance to trypsin digestion was not seen when the TrK13-WT protein was incubated with PPIX or
161 Zn-PPIX or iron salts (ferrous ammonium sulfate, FAS or ferric ammonium sulfate, FES, although
162 these salts are known to bind K13)[24]. Together, these data suggest that heme binding to K13 shows
163 chemical and molecular specificity, may induce confirmational change and thereby induce
164 stabilization of K13 in cells.

165 **K13-regulated oxidative stress responses are triggered by heme**

166 Nuclear factor erythroid 2-related factor 2 (Nrf2) is a major redox-regulated transcription factor
167 controlled by KEAP1[49], the closest mammalian orthologue of K13. We therefore assessed whether
168 Nrf2 was regulated by K13 and the impact of heme, a known, major redox regulator[50]. First, we
169 investigated changes in Nrf2 levels in GFP or KEAP1 expressing cells under HDM or heme-
170 replenished culture conditions *i.e.,* GFP^{HDM} *versus* GFP^{HEME} or $KEAP1^{HDM}$ *versus* $KEAP1^{HEME}$ cells.
171 Relative intensities of both GFP and KEAP1 proteins remained unaffected by heme (**Supplementary**
172 **Fig. 3a, b**). Consequently, we investigated only K13-GFP cells, cultured in the absence or presence
173 of increasing concentrations of heme, and followed by immunoprecipitations from cellular lysates

174 using anti-GFP antibodies. Western blot (**Fig. 2a**) and quantitative densitometric analysis (**Fig. 2b**) of
175 band intensities revealed increasing amounts of immunoprecipitated K13-GFP with increased heme
176 concentrations (**2a i** and **2b i**). In contrast, levels of co-immunopurified Nrf2 decreased with increasing
177 heme (**Fig. 2a i**), although there was increase in the overall cellular Nrf2 levels (**Fig. 2a ii** and **2b ii-**
178 **iii**). These results strongly implied that interactions between K13 and Nrf2 were negatively affected by
179 heme. To investigate whether these reflected direct protein-protein interactions, we co-incubated
180 recombinant Nrf2-6×his protein with either heme-free or heme-bound recombinant TrK13-WT (that
181 was desalted to remove excess unbound heme). As shown in **Fig. 2c**, after incubation with heme for
182 1 h, there was ~26% reduction in Nrf2-6×his binding to TrK13-WT, suggesting heme may directly
183 prevent/disrupt Nrf2 binding to K13.

184 We next performed immunolocalization studies to determine subcellular distribution of Nrf2 in K13-
185 GFP^{HDM} and K13-GFP^{HEME} cells (**Fig. 2d**). Here, data revealed predominantly cytoplasmic localization
186 of Nrf2 with K13-GFP under HDM conditions (left panel). In contrast, the K13-GFP^{HEME} cells displayed
187 prominent nuclear localized Nrf2 protein (right panel). Moreover, in the presence of heme, levels of
188 K13 were higher than under HDM conditions. Subcellular fractionation confirmed that under
189 conditions of HDM, a vast majority (~83%) of Nrf2 protein was detected in the cytoplasmic fraction
190 (**Fig. 2e**; second blot). However, in the K13-GFP^{HEME} cells, ~87% of the Nrf2 protein was detected in
191 the nuclear fraction. As expected, the K13-GFP protein was present exclusively in the cytoplasmic
192 fraction independent of the absence or presence of heme. Furthermore, the intensity of K13-GFP was
193 much higher under heme-replenished condition (top blot). The GFP expressing cells revealed no
194 changes in the relative nuclear/cytoplasmic fractionation of the Nrf2 protein or intensities of GFP
195 (**Supplementary Fig. 3c**). As Nrf2 is a redox-controlled transcription factor, we also compared the
196 expression of stress-response genes *heme oxygenase* (*ho-1*), *NAD(P)H quinone oxidoreductase 1*
197 (*nqo1*) and *thioredoxin reductase 1* (*txnrd1*) in K13-GFP^{HDM} and K13-GFP^{HEME} cells. As shown in **Fig.**
198 **2f**, RT-qPCR data confirmed increased expression of these stress-response genes as a consequence
199 of increased Nrf2 translocation to the cell nucleus.

200 **Chaperone mediate autophagy is a major pathway of K13 degradation**

201 A recent study implicated chaperone-mediated autophagy (CMA) in the lysosomal degradation
202 KEAP1 in mouse midbrain progenitor cell line SN4741[51]. Since K13 shares structural and sequence

203 identity with KEAP1, we investigated if similar degradation pathway was involved in the proteolysis of
204 K13-GFP under HDM conditions. Our analyses of the primary sequence of K13, suggested it
205 contained 'KFERQ-like' motifs as recognized by an online algorithm KFERQ finder v0.8
206 (*https://rshine.einsteinmed.edu*)[52]. These motifs are targeting signals of CMA. In CMA the chaperone
207 heat shock 70-kDa (cognate) protein 8 (also known as HSPA8) binds 'substrate' proteins bearing
208 'KFERQ-like' motifs[53,54]. LAMP2A acts as a receptor on the lysosomal membrane. HSPA8 binds the
209 cytosolic tail of LAMP2A[55]. This in turn unfolds the substrate and enables its translocation into
210 lysosomes where it is subsequently degraded[56]. As shown in **Fig. 3a**, K13 contains eighteen 'KFERQ-
211 like' motif, strongly suggesting it may be targeted to lysosomes. Immunolocalization studies using
212 indirect IFA suggested moderate association between K13 and LAMP2A with Pearson's correlation
213 coefficient (PCC) of 0.59. Notably, heme raised the PCC to 0.79, suggesting it induced a high level of
214 co-association of K13-GFP with LAMP2A (**Fig. 3b**). We therefore concluded that although heme
215 induces conformational change in K13, this does not obscure targeting of K13-GFP to LAMP2A
216 labeled lysosomes. But since heme increases levels of K13, it is not likely to promote degradation of
217 K13-GFP within the lysosome. We therefore propose (as schematic in **Fig. 3b**) that the heme-induced
218 conformational stability may prevent unfolding of the K13-GFP substrate and its translocation into the
219 lysosome, thereby limiting its degradation in cells**.**

220 Since LAMP2A is an exclusive CMA marker, we investigated the effects of a previously reported
221 CMA-inhibitor, *i.e.*, the RARα (retinoic acid receptor alpha) activator ATRA (*all-trans* retinoic acid),
222 known to be a potent inhibitor of LAMP2A expression[57]. As expected, under HDM conditions, there
223 was moderate co-association of K13 and LAMP2A, with a PCC of 0.58 (**Fig. 4a i**). Treatment with
224 ATRA elevated levels of K13-GFP as well as its co-association with LAMP2A (raising the PCC to
225 0.90; **Fig. 4a ii**). As expected, heme also increased K13-GFP levels and the PCC with LAMP2A rose
226 to 0.77 (**Fig. 4a iii**). Notably, ATRA markedly increased K13-GFP in HDM to levels far higher than
227 those seen with heme replenishment (**Fig. 4b i** and **4b iii**). ATRA also significantly reduced LAMP2A
228 levels compared to controls, both in K13-GFP^{HDM} and K13-GFP^{HEME} cells (**Fig. 4b i** and **4b ii**).
229 Together these data strongly suggested ATRA-mediated reduction of LAMP2A prevented the
230 degradation of K13, explaining why it increased K13 levels more than heme.

231 To further confirm the role of LAMP2A-mediated degradation of K13-GFP, we obtained stable
232 transgenic cell lines expressing K13-GFP or GFP in the HeLa *lamp2a* knockout (*Δlamp2a*; Abcam;
233 ab255402) and the corresponding parental HeLa cells (Abcam, ab255928). HeLa cells have
234 previously been reported to inherently express very low levels of native KEAP1 protein and
235 correspondingly have high basal Nrf2 activity[58]. We designated them as *Δlamp2a*$^{K13\text{-}GFP}$, HeLa$^{K13\text{-}GFP}$,
236 *Δlamp2a*^{GFP} and HeLa^{GFP}, cells, respectively. As shown in **Supplementary Fig. 4a**, LAMP2A protein
237 was undetectable in *Δlamp2a* cells both by fluorescence microscopy and in western blots. Moreover,
238 there was no difference in levels of K13-GFP in the transgenic *Δlamp2a*$^{K13\text{-}GFP}$ cells regardless of
239 whether they were cultured under HDM or 5 μM heme-supplemented conditions (**Fig. 4c**). In contrast,
240 significant reduction in the K13-GFP level was evident in the parental HeLa$^{K13\text{-}GFP}$ cells in HDM
241 (compare lanes 3 and lane 4). In *Δlamp2a*^{GFP} cells, we observed no changes in the level of GFP
242 (**Supplementary Fig. 4b**) when compared to the HeLa^{GFP} cells irrespective of HDM or heme-
243 replenished conditions. Thus, the absence of LAMP2A adversely affected the proteolysis of K13-GFP,
244 but not GFP, which further substantiated the involvement of CMA pathway in proteolysis of K13-GFP
245 under HDM conditions.

246 **K13's kelch domain transfers heme-dependent stability and heme binding property to KEAP1**

247 We next investigated if the heme-regulated stability of K13 was due to its kelch repeat (KRP) domain
248 and could be transferred to KEAP1. As shown in **Fig. 5a**, we made chimeras of the N-terminus of
249 KEAP1 and the kelch domain of K13 fused to GFP (KEAP1^{N}K13^{KRP}-GFP) as well N-terminus of K13
250 and the kelch domain of KEAP1 fused to GFP (K13^{N}KEAP1^{KRP}-GFP). Stable expression of
251 KEAP1^{N}K13^{KRP}-GFP and K13^{N}KEAP1^{KRP}-GFP proteins in Du145 cells were confirmed by western
252 blots (**Fig. 5b**). As shown in **Fig. 5c**, immunolabeling assays revealed significant (72%) reduction in
253 KEAP1^{N}K13^{KRP}-GFP cells under HDM conditions when compared to respective counterparts in 5 μM
254 heme-supplemented media. In contrast K13^{N}KEAP1^{KRP}-GFP cells were reduced by only 30%.
255 Supplementing HDM with the heme precursor ALA had no significant effect, but heme largely restored
256 levels of KEAP1^{N}K13^{KRP}-GFP expression (**Fig. 5d)**. K13^{N}KEAP1^{KRP}-GFP showed much less heme-
257 responsive expression (**Fig. 5e**). Together, these results suggested that the kelch domain of K13
258 conferred robust heme-stimulated expression of the KEAP1-K13 chimera which was closely

259 comparable to the wild-type K13-GFP. The NTR, CCD and BTB-POZ domains of K13 also made a
260 minor contribution in transferring heme-dependent phenotype to the KEAP1 chimera.

261 In addition, we investigated the relative affinity of recombinant K13 (also known as TrK13-WT),
262 KEAP1, KEAP1^{N}K13^{KRP} and K13^{N}KEAP1^{KRP} proteins for hemin-agarose. Recombinant proteins
263 expressed and purified from *E. coli* were incubated with hemin-agarose beads and percentage
264 binding was determined (see *Materials and Methods*). As shown in **Fig. 5f**, K13/TrK13-WT, KEAP1,
265 KEAP1^{N}K13^{KRP} K13^{N}KEAP1^{KRP} proteins respectively showed 30.1%, 5.9%, 32.5% and 10.3% binding
266 to hemin-agarose, respectively. Again, this suggested that the kelch domain of K13 could confer the
267 same efficiency of heme binding to KEAP1 as seen associated with K13/TrK13-WT protein. When
268 soluble cellular extracts from stable transgenic Du145 cells ectopically expressing the K13-GFP,
269 KEAP1 and their chimera proteins were used, we again found that K13-GFP, KEAP1,
270 KEAP1^{N}K13^{KRP}-GFP and K13^{N}KEAP1^{KRP}-GFP bound hemin-agarose beads with efficiencies of
271 58.9%, 3.1%, 64.5% and 29.3%, respectively (**Fig. 5g**). Cumulatively, the results in **Fig. 5** strongly
272 support that the kelch domain of K13 transfers robust heme binding capacity and heme-based
273 stabilization to KEAP1. The N-terminal domains of K13 may also contribute a minor role consistent
274 with our prior studies suggesting a subset of heme binding motifs are also detected outside of K13's
275 Kelch domain[24].

276 **K13 and its chimeras confer sensitivity to heme-dependent ART-killing of Du145 cells**

277 Since heme is implicated in the activation of ART, we next assessed the ART sensitivity of Du145
278 cells expressing K13-GFP and its chimeras (as well as GFP alone) in a standard killing MTT [3-(4,5-
279 dimethylthiazol-2-yl)-2,5-diphenyltetrazolium bromide] assay (see *Materials and Methods*) comparing
280 outcomes in HDM or media replenished with 5 μM heme. Du145 cells expressing control GFP
281 showed an IC_{50} of 117.7 ± 0.9 μM in the absence of added heme (**Fig. 6a i**), thereby indicating that
282 they are intrinsically highly resistant to ART. The addition of 5 μM heme minimally reduced the IC_{50} by
283 2.6%. Expression of KEAP1 also showed a small effect inducing approximately 6.1% reduction.
284 However, K13-GFP and the KEAP1^{N}K13^{KRP} cells had a greater effect, which translated into increasing
285 heme-dependent sensitivity to ART by 18.2% and 23.7%, respectively (**Fig. 6a i-ii**). K13^{N}KEAP1^{KRP}-
286 GFP had lesser effect showing ART sensitivity increase of 13.5%. The relative order of conferring
287 increased ART sensitivity was KEAP1^{N}K13^{KRP}-GFP > K13-GFP > K13^{N}KEAP1^{KRP}-GFP > KEAP1 >

288 GFP, which matched the heme binding properties reported for these transgenes in **Fig. 5**. Together,
289 these data suggested that the presence of K13, particularly its kelch domain, conferred sensitivity to
290 ART in the presence of 5 μM heme.

291 Since the K13 also binds Nrf2 (which is antagonized by heme), we examined the effects of ART on
292 the dynamics of K13 and Nrf2 in HDM as well as after heme supplementation. As shown in **Fig. 6b i-**
293 **ii,** ART had no sizeable effect on K13-GFP levels in the presence or absence of heme. However, Nrf2
294 levels were reduced by 50% in the presence of both ART and heme. This reduction was due to the
295 depletion of Nrf2 in the cytoplasm (**Fig. 6c i-ii**), suggesting it was through regulation by K13. These
296 data support a model shown in **Fig. 6d**, where heme plays a major role in binding K13 to displace
297 Nrf2, which in turn is targeted to the nucleus to induce a protective redox (or pro-survival) response.
298 Heme bound to K13 activates ART to generate toxic heme-ART adducts. K13's renewed ability to
299 regulate Nrf2 suggests that these toxic heme-ART adducts do not inactivate K13. Rather, the adducts
300 dislodge from K13 and disperse to mediate damage which occurs in absence of a protective redox
301 response, resulting in cell death (or pro-death) responses. Thus, ART-induced killing reconstituted in
302 Du145 cells may arise from the dual effect of inducing toxic ART-heme adducts as well as preventing
303 a protective redox response to render an overall 'pro-death response (**Fig. 6d**).

304 **ART sensitivity is increased proportional to the K13 intensity**

305 Our findings in **Fig. 6** strongly supported that expression of K13 or chimeras, containing its kelch
306 domain in presence of 5 μM heme, increased sensitivity to ART. We wanted to gain better
307 understanding on whether increasing K13 at sub-micromolar heme concentration also played a role.
308 Since our studies in **Fig. 4** established that ATRA increased levels of K13, we separately evaluated
309 the effects of heme and ATRA. As shown in **Fig. 7a, b**, in cells expressing GFP, 5 μM heme
310 increased sensitivity to ART by ~ 6%, while ATRA had no effect. In K13-GFP cells, heme alone
311 stimulated ART-sensitivity by 18%, ATRA by 25%, and the combination of two stimulated ART-
312 sensitivity by 36% (**Fig. 7a, b**). These data strongly suggested that elevation in levels of K13-GFP by
313 ATRA even under HDM conditions increased sensitivity to ART. But heme at 5 μM provided additional
314 sensitization effect possibly by (i) increasing K13 levels (ii) providing substrate to form toxic heme-
315 ART adducts, whose disassociation from K13 suppression of pro-survival responses (as hypothesized
316 in **Fig. 6d**).

317 We were therefore interested in determining whether ART sensitivity was proportional to K13
318 intensity. To do so, we compared the sensitivity to killing by ART to levels of K13 (or its kelch chimera)
319 normalized to GAPDH (a control cytoplasmic protein). As shown in **Fig. 7c**, we observed an overall
320 linear relationship between increase in ART sensitivity and the K13/GAPDH (R^2 value = 0.97).
321 Notably, cell lines designated as 1, 2 and 4 reflected measurements generated in HDM, and all
322 showed lower degree of ART sensitivity and K13/GAPDH levels than counterpart measurements
323 generated in the presence of 5 μM heme. Also, the presence of ATRA increased K13 levels, thereby
324 boosting K13/GAPDH ratio and correspondingly showed increased ART sensitivity of K13-GFP cells
325 under HDM conditions (as cell line #3 in **Fig. 7c**). Moreover, combination of heme and ATRA in these
326 cells (designated as 3H) further elevated K13/GAPDH ratio and showed highest sensitivity to ART
327 (38%). Comparisons in HeLa cells revealed that knockout of LAMP2A, which increased K13/GAPDH
328 by three-fold raised ART sensitivity by one-third. However, 5 μM heme further raised the K13/GAPDH
329 ratio four-fold and doubled ART-sensitivity (compared to parental HeLa in HDM).

330 When we separately compared the effects of extracellular 5 μM *versus* 50 μM heme (**Fig. 7d**), the
331 higher concentration of heme further augmented killing. In GFP cells, this could be easily interpretable
332 as increasing intracellular heme alone from ~400 to 750 nM directly sensitized ART-killing, increasing
333 it from ~2 to ~6%. However, as we have previously shown for K13 kelch domain proteins, heme may
334 also act by raising levels of the transgene alone. We therefore tracked transgene expression at 50 μM
335 heme (**Fig. 7d**, black bars). This revealed that even at 50 μM, increasing K13-GFP and K13 chimeras
336 stimulated ART-killing to much higher levels. Taken together, these data suggest that heme alone (at
337 intracellular concentrations of 400 nM to 1 μM), is comparatively weak stimulator of ART's killing
338 activity but can be potentiated by expression of K13 and its appropriate chimeras.

339 **Discussion**

340 K13 was identified as marker of ART-R more than a decade ago[6]. Our studies provide the first
341 evidence that it acts as redox sensor regulated by the oxidant heme (summarized in **Fig. 8a**). This is
342 also the first report that a small molecule like heme can bind a member of an evolutionary conserved
343 kelch family (whilst multiple protein partners have been defined for kelch proteins[15,59–61]). Notably,
344 K13-heme activates ARTs, suggesting the potent killing action of these drugs exploits a parasite
345 protective redox response (**Fig. 8a, cycle 1**) Whether *Plasmodium* encodes for functional orthologue

346 of Nrf2 (the transcription factor that induces the stress-induced protective response in Du145 cells)
347 remains unknown. However, since heme is a strong oxidant[31], upon its binding to K13, a protective
348 redox response is likely elicited as a compensatory effect (expected for **cycles 2 and 3** shown in **Fig.**
349 **8a**). A redox stress response may be needed to protect the parasite against high levels of heme
350 reported at all stages of parasite growth[62].

351 The models in **Fig. 8a, b** maybe particularly informative for clinically reported ART-induced ring-stage
352 death[63,64] based on the following considerations. Young rings (0-3 h) lack a digestive food vacuole
353 and therefore depend on heme from biosynthetic sources, analogous to Du145 cells. Similarly in *P.*
354 *falciparum* rings, K13-heme triggers a pro-survival response exploited by ART to spring a pro-death
355 response of oxidizing ART-heme adducts that are no longer redox active but can kill the ring parasite
356 (**Fig. 8b i**), and this function is compromised in ART-R (**Fig. 8b ii**). To date, K13 function has been
357 best understood in context of regulation of uptake of hemoglobin into the food vacuole at the
358 trophozoite stage. However, it is well documented that K13 is expressed in daughter merozoites that
359 assemble when trophozoites mature to the segmented schizont stage. K13 is also detected from the
360 earliest stages of ring infection (mode in **Fig. 8b ii**)[59,65,66]. However, K13's precise location is not well
361 mapped in *P. falciparum* merozoites and rings. But in the related apicomplexan *Toxoplasma gondii*, a
362 K13 orthologue was localized to endosomal structures called Type I micropores and shown to
363 regulate plasma membrane endocytosis[67,68]. Since all apicomplexans (including *Plasmodium*) contain
364 a 'Type I' micropore in their 'apical' stages[69,70], by virtue of evolutionary conservation of mechanisms
365 of apical organelles, we have proposed that in merozoites and rings K13 localizes to *P. falciparum*
366 Type I micropores and regulates essential plasma membrane endocytic functions of these parasite
367 stages [71] (**Fig. 8b i**). Indeed the *P. falciparum* food vacuole where K13 is abundant develops from a
368 Type II micropore, which is also consistent with a conserved micropore function for K13.

369 The Du145 cell model enabled assessment of the effects of K13 binding to heme from nanomolar to
370 sub-micromolar range. The intrinsic concentration of heme in Du145 cells is 60 nM. Supplementing
371 with extracellular heme at 5 μM and 50 μM resulted in maximal intracellular concentrations of 0.45 μM
372 and 0.75 μM, which approach but are nonetheless lower than the published physiological range (1-5
373 μM) reported for *Plasmodium*[40,41]. Whether kelch proteins of other apicomplexans bind heme has yet
374 to be investigated. Moreover, although the kelch domain of K13 is necessary and sufficient to confer

375 heme binding property to its closest mammalian orthologue KEAP1, whether and how heme is
376 released from K13 under physiological conditions is not known, since it cannot be ubiquitinylated and
377 degraded, which is a hallmark of protein substrates and their cellular regulation by kelch proteins. But
378 our studies suggest that when K13-bound heme activates ART, the kelch structure may protect
379 against self-oxidation by heme-ART adducts[24]. This is consistent with prior studies showing that
380 alkyne-ART analog despite being highly active against a wide range of malarial cellular targets failed
381 to alkylate K13[72,73]. Heme-ART adducts show low affinity for recombinant K13[24], suggesting a
382 mechanism for their release and a new model where a single molecule of K13 may catalyze multiple
383 cycles of heme-ART toxic adduct formation and oxidative killing (**Fig. 8a**; K13 cycle 1).

384 That we find that intracellular heme concentrations of 400- 750 nM alone yield low sensitization to
385 ART, counters prevailing models that suggest that heme alone is sufficient to activate a low level of
386 ART at the trophozoite stages (**Fig. 8c**). Notably, our data show that even at the lowest intensities,
387 K13 (expected not to exceed nanomolar levels) was more effective than heme alone and in addition,
388 the extent of sensitization was directly proportional to the level of K13. This is consistent with our
389 findings that raising K13 (by ATRA treatment) in HDM increased ART-sensitivity more than an eight-
390 fold in free heme concentrations of 60 nM. These data strongly support the idea that K13 acts as
391 'catalyst' to facilitate assembly of activated ART-heme complexes, and once the activated toxic
392 adducts are released, K13 may facilitate successive rounds of ART-based killing. We therefore
393 propose that even at the trophozoite stage, rather than heme alone, it is the K13-bound heme which
394 effects sensitization to ART (**Fig. 8c**). These stages are known to be far more sensitive to ART than
395 rings, and trophozoites expressing K13 mutations of ART-R are highly susceptible to killing by ART,
396 which is consistent with their higher levels of K13.

397 K13-heme concentration at late endosomes in Du145 cells suggests that in addition to triggering a
398 pro-survival response, heme binding to K13 may stabilize endosomal location in both rings and
399 trophozoites and possibly create concentrated cellular foci of K13 function as well as efficiently
400 activate ART at all stages of parasite growth. That heme binding, endosomal concentration and ART-
401 based killing are not properties of mammalian KEAP1, suggests they are parasite evolutionary
402 adaptations conferred by the K13 kelch domain. Yet, orthologues of LAMP2A (a receptor for K13 in
403 Du145 and HeLa cells that controls its autophagic degradation), have not been reported in *P.*

404 *falciparum* or *T. gondii.* Nonetheless, autophagic systems exist in both parasites[74,75] and additional
405 studies are needed to determine their influence on heme-dependent K13 stability, as well as
406 endosomal degradation and turnover of K13 and its orthologues across apicomplexans. Another key
407 priority is identification of K13-coupled parasite redox factors that remain unidentified because a lack
408 of conservation at the level of primary sequences prevents easy prediction from nucleotide sequence
409 comparisons. While our studies establish that K13 is an important determinant in ART sensitization,
410 other redox and oxidative factors may also play a role. Our data suggest Du145 may continue to
411 provide a powerful model system for future functional screens of endosomal effectors as well as novel
412 plasmodial pro-oxidant responses, regulated by both heme and K13 and targeted in killing by ART.
413 One generalized lesson already learned may be that suppression of redox sensing may sensitize a
414 wider range of infectious agents as well as cancers to killing by ARTs.

415 **Materials and methods**

416 **Generation of plasmid constructs**

417 The pPR-IBA101 (TrK13-WT) plasmid was generated as described in earlier studies[24,47]. For the
418 generation of pPR-IBA101 (KEAP1), the full length (1875 base pairs) transcript of *keap1* was
419 amplified from cDNA library prepared from human cell line (HEK293T) using the primer pairs (Hs-
420 Keap1-BsaI-Fwd (5'-CAAATGGGAGACCTTATGCAGCCAGATCCCAGGC-3') and Hs-Keap1-BsaI-
421 Rev (5'-CCAAGCGCTGAGACCAGCAGCACAGGTACAGTTCTGCTGGTCAATCTG-3'). The PCR
422 product was digested with BsaI and cloned at corresponding sites in similarly digested pPR-IBA101.
423 For the generation of pPR-IBA101 (KEAP1^{N}K13^{KRP}), nucleotide sequences coding for the N-terminus
424 region of KEAP1 was amplified from pPR-IBA101 (KEAP1) plasmid using (Hs-Keap1-BsaI-Fwd and
425 KEAP1toK13-KRP-Rev (5'-AAATCCACCGGCAGCAGCGCGGCCCACCTTGGG-3') primers.
426 Nucleotide sequence encoding for the KRP region of K13 was amplified using the pPR-IBA101
427 (TrK13-WT) plasmid as template and KEAP1toK13-KRP-Fwd (5'-
428 GTGGGCCGCGCTGCTGCCGGTGGATTTGATGGTGTAGAATATTTAAATTCG-3') and PfKelch13-
429 BsaI-Rev (5'-GGAGGACAAAATGGCAATGTTCTAAATTCATGTGGATTCTTTTCACCAGAT
430 ACAAATGAATGGC-3') primer pairs. The two PCR products were used as templates to reconstitute
431 KEAP1^{N}K13^{KRP} by overlapping PCR, which was then digested with BsaI and cloned into pPR-IBA101.
432 Similarly, to generate pPR-IBA101 (K13^{N}KEAP1^{KRP}), nucleotide sequences encoding for the N-

433 terminus of K13 was amplified from pPR-IBA101 (TrK13-WT) plasmid as template and PfKelch13-
434 BsaI-Fwd (5'-
435 CAAATGGGAGACCTTATGGAAGGAGAAAAAGTAAAAACAAAAGCAAATAGTATCTCG-3') and
436 K13toKEAP1-KRP-Rev (5'-GTAGATCAG
437 GGCAGCAGCTATACAAAATACTAATGGGAATGGTAAAAATTTAATACC-3') primers. Overlapping
438 PCR, using the above two PCR products as templates, generated $K13^{N}KEAP1^{KRP}$ which then
439 introduced to pPR-IBA101 after digestion with BsaI.
440 For generating recombinant Nrf2-6×his, the full length (1626 bp) transcript was amplified from cDNA
441 library prepared from human cell line (Du145) using the primer pairs HsNrf2-XbaIFwd (5'-
442 CACGTGTCTAGAATGATGGACTTGGAGCTGCCG-3') and HsNrf2ns-XhoIRev (5'-
443 CCTAGGCTCGAGGTTTTTCTTAACATCTGGCTTCTTACTTTTGGG-3') and the PCR product was
444 then digested with XbaI-XhoI and clone into similarly digested pET303-ct-his plasmid (ThermoFisher,
445 USA) for in-frame fusion with C-terminus 6×his tag. To generate GFP expressing constructs for
446 mammalian cells, pAcGFP1-C1 (Addgene, USA) was used and AgeI and NheI sites considered for
447 inserting the gene of interest. To generate pAcGFP1-C1 (K13-GFP), pAcGFP1-C1 ($KEAP1^{N}K13^{KRP}$)
448 and pAcGFP1-C1 ($K13^{N}KEAP1^{KRP}$) plasmids, their pPR-IBA101 plasmids were used as
449 corresponding templates. For K13-GFP, the primers pairs were PfKelch13-NheI-Fwd (5'-
450 AAGCTTGCTAGCATGAACAGCGAGGTGTGTTCGCG-3') and PfKelch13-AgeI-Rev (5'-
451 AGCGCTACCGGTAGCAGCCAAATTTGCCAAGAGAATGCCGTG-3'), for generating
452 $KEAP1^{N}K13^{KRP}GFP$, the primer pairs were KEAP1-NheI-Fwd (5'-
453 AGATCTGCTAGCATGCAGCCAGATCCCAGGC-3') and PfKelch13-AgeI-Rev (5'-
454 AGCGCTACCGGTAGCAGCCAAATTTGCCAAGAGAATGCCGTG-3'); and for generating
455 $K13^{N}KEAP1^{KRP}$, PfKelch13-NheI-Fwd (5'-AAGCTTGCTAGCATGAACAGCGAGGTGTGTTCGCG-3')
456 and KEAP1-AAA-AgeIRev (5'-GGATCCACCGGTAGCTGCTGCACAGGTACAGTTCTGC
457 TGGTCAATC-3') primers were used. To generate the KEAP1 construct, pPR-IBA101 (KEAP1)
458 plasmid was used as the template to amplify nucleotides encoding for KEAP1-strep using KEAP1-
459 NheI-Fwd and Strep-XhoI-Rev (5'-GGATCCCTCGAGCTTTCTCGAACTGCGGGTGGCTCCAA-3').
460 The PCR amplified product was subjected to NheI-XhoI digestion and inserted into similarly digested
461 pAcGFP1-C1.

462 All constructs generated for this study were confirmed by Sanger's sequencing prior to further
463 experiments.

464 **Cell culture, generation of transgenic lines and their treatments**

465 The Du145 cell line was the kind gift from Prof. Rana Pratap Singh, SLS, JNU, India. The parental
466 HeLa (ab255928) and HeLa-Δ*lamp2a* (ab255402) were procured from Abcam, USA and cultured
467 according to the manufacturer's instructions in complete media RPMI (Gibco, USA). Cells were
468 transfected using Lipofectamine 3000 (Invitrogen, USA) following the manufacturer protocol. Stable
469 transgenic lines were generated by G418 (0.5 mg/ml, Sigma, USA) selection. For the heme depleted
470 (HDM) conditions, the cells were grown in RPMI media supplemented with heme-depleted FBS and
471 succinyl acetone (0.5 mM, Caymanchem, USA) for 48 h. For heme-replenished media 5 μM hemin
472 chloride (Merck, USA) was added to the HDM. To assess *in vivo* stability of K13 protein upon heme
473 binding, the cells were treated with heme analogs PPIX (50 μM, Merck, USA) or Zn-PPIX (50 μM,
474 Merck, USA) for 48 h. Cells were also subjected to treatment either with for 48 h with ART (50 μM,
475 Caymanchem, USA) in presence or absence of heme.

476 **Preparation of heme-depleted FBS**

477 Commercially purchased FBS (Gibco, USA) was incubated with ascorbic acid (10 mM, SRL, India) at
478 37°C in a shaking incubator at 200 rpm for overnight. Spectral scans of the pre- and post-treated FBS
479 measured to check the presence or absence of soret peak at 410 nm, respectively using JASCO
480 UV660 spectrophotometer. Finally, the ascorbate-treated FBS was dialyzed against PBS, pH 7.4, with
481 at least three periodic changes for 24 h at 4°C. Dialyzed FBS was filter-sterilized using 0.2 μm
482 polyether sulfone filter (Sartorius, USA).

483 **Assessment of cellular viability**

484 Cell viability was assessed using 3-(4,5-dimethylthiazol-2-yl)-2,5-diphenyltetrazolium bromide (MTT,
485 Merck, USA)-based colorimetric assay. Cells at 50-60% confluency and within 72 h incubation in the
486 96-well cell culture plate were only considered. Following treatment, the cells incubated with 20 μl of 5
487 mg/ml MTT solution for 2h at 37° in the dark. Finally, the culture media was discarded, and formazan
488 crystal was dissolved with 200 μl of DMSO, and absorbance was recorded at 570 nm using a
489 microplate reader (Thermo Fisher Scientific, USA). Cell viability was calculated and expressed as
490 percentage in comparison to the untreated controls. For MTT assay, the viability was calculated for

491 six different concentrations (0, 40, 80, 120, 160 and 200 μM) in three replicates to generate the IC_{50}
492 values for ART.

493 **Estimation of total cellular heme content**

494 Cells were grown up to 90-95% confluency and dislodged from the plate by treatment with trypsin and
495 were washed twice with saline PBS. Cell count was recorded prior to lysis using hemocytometer.
496 Cells were then solubilized in five volumes of RIPA buffer for 2 h at 4ºC. After a brief centrifugation,
497 the supernatant was diluted ten times and subjected for spectrophotometric scanning at 410 nm. The
498 absorbance was plotted against the standard curve of hemin chloride to calculate the total cellular
499 heme content. The standard curve has been generated using gradually increasing concentration (0,
500 0.05, 0.1, 0.5, 1 and 10 μM) of hemin chloride.

501 **Nuclear and cytoplasmic fractionation of transgenic cells**

502 Cellular fractionation into nuclear and cytoplasmic fractions was performed following previously
503 described protocol[76]. Briefly, the cells from the 60 mm culture plates were scrapped and washed twice
504 with ice-cold phosphate buffered saline (PBS) pH 7.4. The cell pellets were washed, resuspended in
505 250 μl of ice-cold 0.2% (v/v) NP40 (HiMedia Labs, India), minced with micro-pestle, vortexed and kept
506 on rocker shaker for 15 mins. The resuspended pellets were then centrifuged at 10,000 rpm for 1 min,
507 and the supernatant was collected as the cytoplasmic fraction. The pellet was then resuspended in 1
508 ml ice-cold 0.2% (v/v) NP40 to remove remnant cytoplasmic debris and centrifuged at same speed.
509 Finally, the pellet was resuspended in 200 μl ice-cold PBS and designated as the nuclear fraction.
510 The nuclear fraction was also briefly sonicated using micro pulser (Sonics, USA).

511 **Indirect immunofluorescence assay (IFA)**

512 IFA was performed using parental or transfected cell lines. Briefly, cells were initially grown on poly-L-
513 lysine coated coverslips and fixed using 4% (w/v) paraformaldehyde/ 0.0075% (v/v) glutaraldehyde
514 followed by permeabilization with 0.1% (v/v) Triton X-100 and neutralized with 50 mM NH_4Cl. Blocking
515 was done using 3% (w/v) BSA. The coverslips were incubated with respective primary antibodies (10
516 μg/ml) at 4°C for overnight followed by incubation in FITC- or TRITC/ Rhodamine-conjugated
517 secondary IgG antibodies (1:200; MP biomedicals, USA). Cellular nuclei were stained with 5 μg/ml
518 Hoechst 33342 (Molecular Probes) and slides were mounted with DABCO. The slides were finally

519 visualized by SP8 confocal laser scanning microscope (Leica, Germany). Fluorescence intensity was
520 calculated using Image-J software (*https://imagej.net/ij/*) software by considering 3 biological
521 replicates for each set and each replicate containing 30 individual cells. The RGB intensity plot and
522 Person's correlation coefficient (PCC) was generated from the Image-J graphics and JaCop,
523 respectively.

524 **SDS-PAGE and western blotting**

525 The induced bacterial cell pellet was directly solubilized in Laemmli's sample buffer and heat
526 denatured for 15 min at 95ºC. For mammalian cells, following scrapping from plates, cells were
527 washed twice with saline PBS and solubilized in five volumes of RIPA buffer for 2 h at 4ºC. After a
528 brief centrifugation, the supernatant was considered as whole protein pool and boiled for 15 min at
529 95ºC using Laemmli's sample buffer and resolved by 8-10% SDS-PAGE followed by Coomassie or
530 silver staining. For subsequent western blots, resolved proteins were transferred into nitrocellulose
531 membrane (MDI, USA) followed by blocking with ice cold 5% (w/v) fat-free skim milk (SRL, India) for 2
532 h at RT. The membranes were incubated with specific primary antibodies (1:3000 to 1:5000 dilution)
533 for overnight at 4ºC on a platform shaker followed by subsequent washing and incubation with
534 respective HRP-conjugated secondary antibodies (1:7000 to 1:10000 dilution). Blots were finally
535 developed by ECL assay and detected using gel imager (Bio-Rad, USA). The primary antibodies are
536 used in this study were: anti-GFP (Invitrogen, USA; Cloud clone, China), anti-UBQ, anti-Lamp2 and
537 anti-GAPDH (Cloud clone, China), anti-k13 (Custom generated, Biobharati Life Sciences[47]), anti-
538 Histone 3 (kind gift from Prof. Suman Kumar Dhar, SCMM, JNU, India), anti-Nrf2, anti-KEAP1, anti-
539 HO1, anti-NQO1, anti-MCM3, anti-DPP3 and anti-TRAF2 (ABclonal, Woburn), anti-His and
540 streptavidin-HRP (BioBharati Life Sciences, India), and anti-HA. The subsequent HRP conjugated
541 secondary antibodies used in this study were goat anti-rabbit (Bio-Rad, USA), goat anti-mouse, goat
542 anti-rat (MP biomedicals, USA). Band intensity was calculated from Image-J (*https://imagej.net/ij/*)
543 software by considering 3 individual blots for each data set.

544 **Purification of recombinant protein and *in vitro* trypsin digestion**

545 Recombinant Trk13-WT, KEAP1, $K13^{N}KEAP1^{KRP}$and $KEAP1^{N}K13^{KRP}$ proteins as C-terminus fusion
546 with strep tag and Nrf2-6×his were purified from isopropyl-1-thio-β-D-galactopyranoside (IPTG, SRL,
547 India) and arabinose (0.2%, SRL, India) induced bacterial pellet. Briefly, the induced bacterial pellet

548 was lysed using lysozyme (SRL, India), sonicated and washed thrice with 2% (w/v) sodium
549 deoxycholate (SRL, India) to purify inclusion bodies (IBs). The IBs were dissolved into 2 M urea, 50
550 mM Tris-HCl buffer pH 12.5 and then dialyzed against buffer W (50 mM Tris-HCl, 150 mM NaCl, pH
551 8). Dialyzed solution was kept for binding to StrepTactin XT Superflow resin (IBA, Germany) for
552 Trk13-WT, KEAP1, $K13^{N}KEAP1^{KRP}$and $KEAP1^{N}K13^{KRP}$ and Ni-NTA resin (Thermo, USA) for Nrf2-
553 6×his. Purified proteins were dialyzed overnight at 4°C against buffer W with at least three periodic
554 changes. Purity of each protein was checked by SDS-PAGE and Coomassie staining and further
555 confirmed by western blotting using commercial antibodies against the 6×his tag, strep tag (Biobharati
556 Life Sciences) or custom-generated anti-K13.

557 For *in vitro* trypsin digestion, 10 µg of recombinant TrK13-WT or commercially procured BSA (A3294,
558 Sigma, USA) was incubated with or without equimolar concentrations of heme in buffer W for 1 h.
559 Samples were desalted as described in our earlier study[24], and treated with 0.5 µg trypsin (T6567,
560 Sigma-Aldrich) for different incubation times. Following digestions, Laemmli's sample buffer was
561 immediately added to each sample, boiled for 15 min at 95˚C and processed for SDS-PAGE and
562 Coomassie staining.

563 ***In vitro* protein-protein interactions**

564 The purified recombinant Nrf2-6×his (10 µM) was incubated with Ni-NTA beads overnight and washed
565 thrice with buffer W containing 30 mM imidazole. The Ni-NTA bound recombinant Nrf2-6×his was
566 then incubated with purified recombinant TrK13-WT (10 µM) in buffer W for 4 h at RT. The beads
567 were thoroughly washed with buffer W, and Ni-NTA-bound proteins were resolved by SDS-PAGE
568 followed by Coomassie staining or western blot using antibodies against the 6×his tag, strep-tag
569 (Biobharati Life Sciences) or custom-generated anti-K13. For experiments involving the interactions
570 between heme-bound or heme-free recombinant TrK13-WT and Nrf2-6×his, the TrK13-WT was
571 preincubated with heme (0 or 10 µM) at RT for 1 h at room temperature (RT) and desalted using PD
572 Spintrap™ G-25 columns (Cytiva) to remove excess unbound heme.

573 **Hemin agarose binding**

574 Affinity-purified recombinant Trk13-WT, KEAP1, $K13^{N}KEAP1^{KRP}$and $KEAP1^{N}K13^{KRP}$ proteins (10 µM)
575 were incubated with 50 µl suspensions of 50% v/v hemin-agarose (Merck, USA) beads for 1 h at RT

576 in buffer W, pH 8, under rotating conditions, followed by five washes with ten volumes of buffer W to
577 remove unbound proteins. The hemin-agarose beads were then solubilized in Laemmli's sample
578 buffer, resolved by SDS-PAGE, and visualized by Coomassie staining. For assessing hemin-agarose
579 binding from transgenic cellular lysates, the total cell pellet was resuspended in 5 volumes of ice-cold
580 RIPA buffer complemented with 1X protease inhibitor cocktail (cOmplete, Roche) and incubated at
581 rotating wheel for 1 h. After centrifugation (15 mins, 21,100 × g, 4ºC), the supernatant containing
582 soluble proteins fractions was incubated with hemin agarose beads for 4 h. Unbound proteins in the
583 lysates were washed with ten volumes of RIPA buffer and bound fractions were then solubilized in
584 Laemmli's sample buffer and subjected to western blotting using anti-strep tag antibody (Biobharati
585 Life Sciences).

586 **Co-immunoprecipitation**

587 Protein A beads (IBA Life Sciences, Germany) were incubated with 10 µg of respective primary
588 antibodies for 4 h at 4 ˚C under rotating conditions and unbound antibodies were removed by
589 extensive washes with pre-cooled PBS. Mammalian cells were harvested, lysed with five volumes of
590 RIPA buffer supplemented with 1 mM PMSF (Thermo, USA) and protease inhibitor cocktail (Roche)
591 and centrifuged at 10,000 × g for 15 min at 4ºC to remove the cell debris. Clarified lysates were then
592 incubated with antibody-coated protein A beads (30-50 µl, 50% v/v resuspension) for overnight at 4ºC
593 under rotating conditions. Following binding, unbound lysates were removed and the beads washed
594 twice with RIPA buffer and twice with ice-cold saline PBS. Beads were boiled with Laemmli's sample
595 buffer for 15 min at 95˚C and processed for western blotting.

596 **Total RNA, cDNA synthesis, and real time RT qPCR**

597 The total RNA was isolated by Trizol reagent (Invitrogen, USA). Briefly, cell pellets were washed twice
598 with PBS and homogenized using 500 µl of Trizol reagent. The supernatants were isolated after a
599 brief centrifugation, mixed with 300 µl chloroform and incubated at RT. After centrifugation at 13,000 ×
600 g for 15 min at 4ºC, the upper aqueous phase was removed and 500 µl isopropanol added. Following
601 incubation for 30 min at RT, the tubes were centrifuged at 13,000 × g for 15 min at 4ºC. The pellet
602 was washed twice with 70% ethanol and finally dissolved in TE. Samples were treated with DNase I
603 enzyme (Thermo scientific, USA) to remove genomic DNA contamination. The quantity and quality of
604 RNA was estimated using Bio spectrophotometer (Eppendorf, Germany) and agarose-formamide gel

605 electrophoresis. Approximately 1 µg of total RNA was used for cDNA synthesis using PrimeScript 1st
606 strand cDNA Synthesis Kit (Takara-Bio, Japan) following manufacturer's protocol. For real time RT-
607 qPCR analyses, 2 µl of ten-fold diluted stock solution of cDNA samples was used. To perform RT-
608 qPCR analyses, primers were designed based on the coding sequence of specific genes using Oligo
609 Analyzer software (*https://eurofinsgenomics.eu/en/ecom/tools/oligo-analysis/*). Primers pairs were
610 HsHO1_RT_Fwd (5'-ATGACACCAAGGACCAGAGC-3') and HsHO1_RT_Rev (5'-
611 GCATAAAGCCCTACAGCAACT-3'); HsNQO1_RT_Fwd (5'-CCTTCCGGAGTAAGAAGGCAG-3') and
612 HsNQO1_RT_Rev (5'-TCCAGGCGTTTCTTCCATCC-3'); HsTXNRD1_RT_Fwd (5'-
613 GGAACTAGATGGGGTCTCGG-3') and HsTXNRD1_RT_Rev (5'-TCTTGCAGGGCTTGTCCTAA-
614 3'). RT-qPCR analyses were performed by using HOTFIRE Pol EvaGreen qPCR Mix Plus (ROX)
615 (Solis BioDyne, USA) and Step one plus system (Applied biosystem, USA). To confirm the absence of
616 any primer dimers in the amplified products, a standard melting curve analysis was conducted.
617 Primers for *gapdh* included HsGAPDH_RT_Fwd (5'-CAGGAGGCATTGCTGATGAT-3') and
618 HsGAPDH_RT_Rev (5'-GAAGGCTGGGGCTCATTT-3') as reference. Relative fold change was
619 calculated by $2^{-\Delta\Delta Ct}$ method.

620 **Statistical validation**

621 One-way ANOVA was carried out to test significance in difference considering at least three biological
622 replicates using GraphPad prism 10. The adjusted p values (p.adj ≤ 0.001) were obtained via Tukey's
623 HSD.

624 **Author contributions**

625 Conceptualization Ideas: S.D., K.H., S.B.[1] and S.B.[2].
626 Methodology: S.D., M.F.
627 Validation: S.D.
628 Investigation: S.D.
629 Resources: S.B.[1], S.B.[2], K.H.
630 Writing: S.D., K.H., S.B.[1]
631 Supervision: K.H., S.B.[1]
632 Project Administration: S.B.[1]
633 Funding acquisition: S.B.[1]

Acknowledgements

This work was supported by research grants from the Indian Council of Medical Research (ICMR), (58/25/2020/PHA/BMS) and Indian Ministry of Human Resource Development (MHRD) Scheme for Translational and Advanced Research in Sciences (STARS) (MoE-STARS/STARS-2/2023-0111) from the Government of India (SB). SD is a recipient of Department of Biotechnology Research Associate fellowship (DBTRA/2023 24/N/JNU/118) from the Government of India.

Funding sources and disclosure of conflicts of interest

The authors declare that the funding source(s) had no role in the study design, data collection, analyses, and interpretation, and in the decision to submit the article for publication. The authors also declare that they have no competing interests related to this manuscript.

Data availability

The authors declare that the source data supporting the findings of this study are available within the paper and the associated supplementary information files (Supplementary Figures 1-4).

Materials & Correspondence

Correspondence and material requests should be addressed to Souvik Bhattacharjee (*souvik@jnu.ac.in*)

Figure and figure legends

Fig. 1

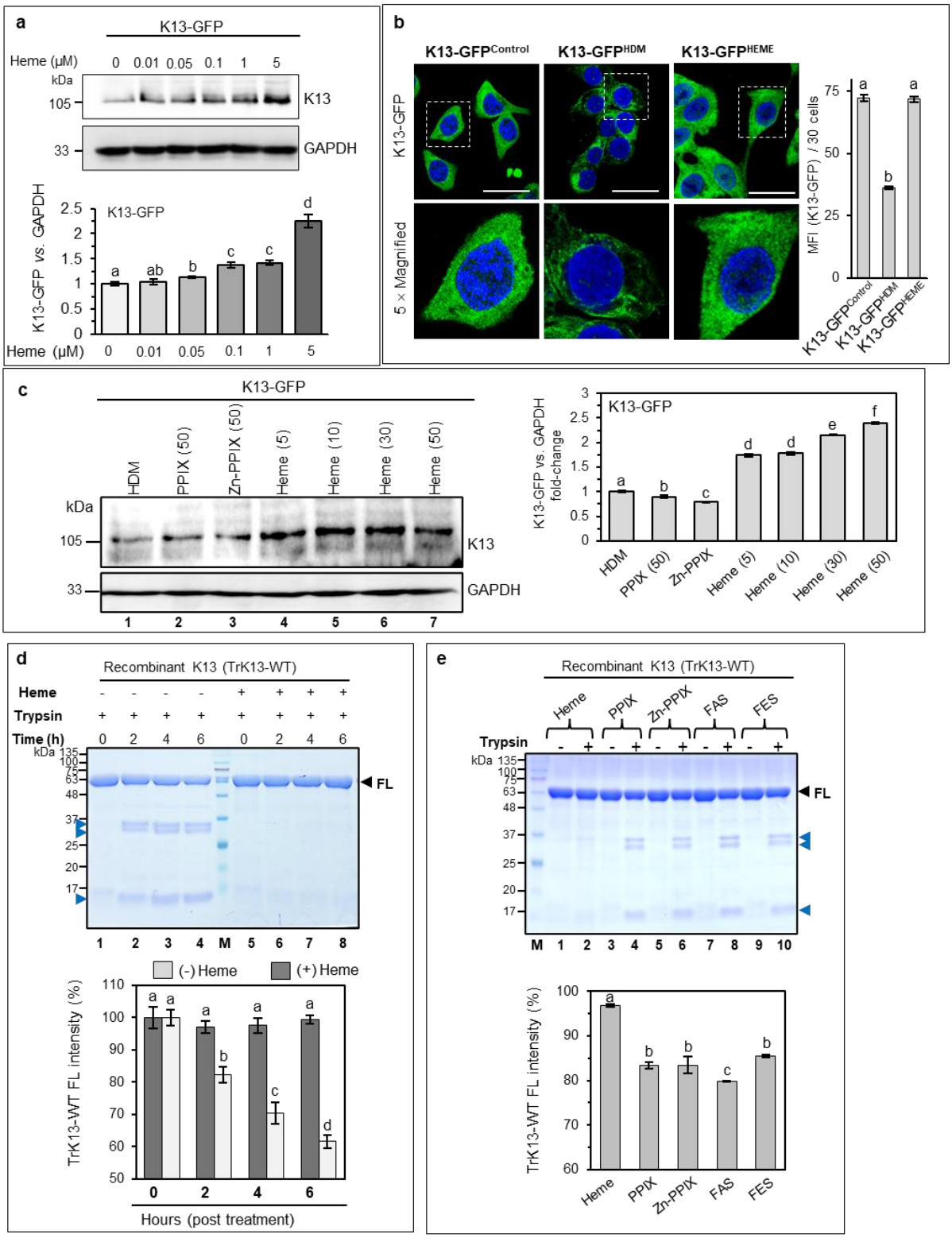

652

653 **Fig. 1. Heme stabilizes K13-GFP and confers *in vitro* resistance to trypsin digestion. a.** Western
654 blots (top) and densitometric analysis (bottom) for K13-GFP under HDM condition or when
655 supplemented with increasing concentrations of heme. GAPDH is the loading control. **b.** IFA images

656 (left) and mean fluorescence intensity plot (MFI, right) of K13-GFP cells under control, HDM or 5 μM
657 heme-supplemented conditions. Scale bar, 5 μm. **c.** Western blot (left) and quantitative densitometric
658 analysis (right) of K13-GFP band intensity under HDM condition (lane 1), or upon supplementation
659 with heme analogs PPIX (lane 2), Zn-PPIX (lane 3) or increasing concentrations (μM) of heme (lanes
660 4-7). Values in parenthesis indicate concentration (in μM). **d.** Coomassie-stained SDS-PAGE showing
661 trypsin-digested fragments (blue arrowheads) derived from the full length (FL, black arrowhead)
662 recombinant K13 (TrK13-WT) in heme-free (lanes 2-4) and heme-bound TrK13-WT (lanes 6-8)
663 protein. The heme-free and heme-bound TrK13-WT proteins without trypsin treatment are shown in
664 lanes 1 and 5, respectively. **e.** Coomassie-stained SDS-PAGE showing trypsin-digested fragments
665 (blue arrowheads) derived from the recombinant FL TrK13-WT protein (black arrowhead) when
666 preincubated with heme analogs PPIX, Zn-PPIX, FAS or FES (lanes 4, 6, 8 and 10, respectively) and
667 not by the heme-bound TrK13-WT (lane 2) protein. Lanes 1, 3, 5, 7 and 9 represent samples with no
668 trypsin treatment. Molecular weight standards (M) for all SDS-PAGE and western blots (in kDa) are as
669 indicated. Graphs represent mean from three biological replicates ± SE. Statistical significance
670 calculated by one-way Anova. Distinct alphabets represent significant difference at p.adj ≤ 0.05.

Fig. 2

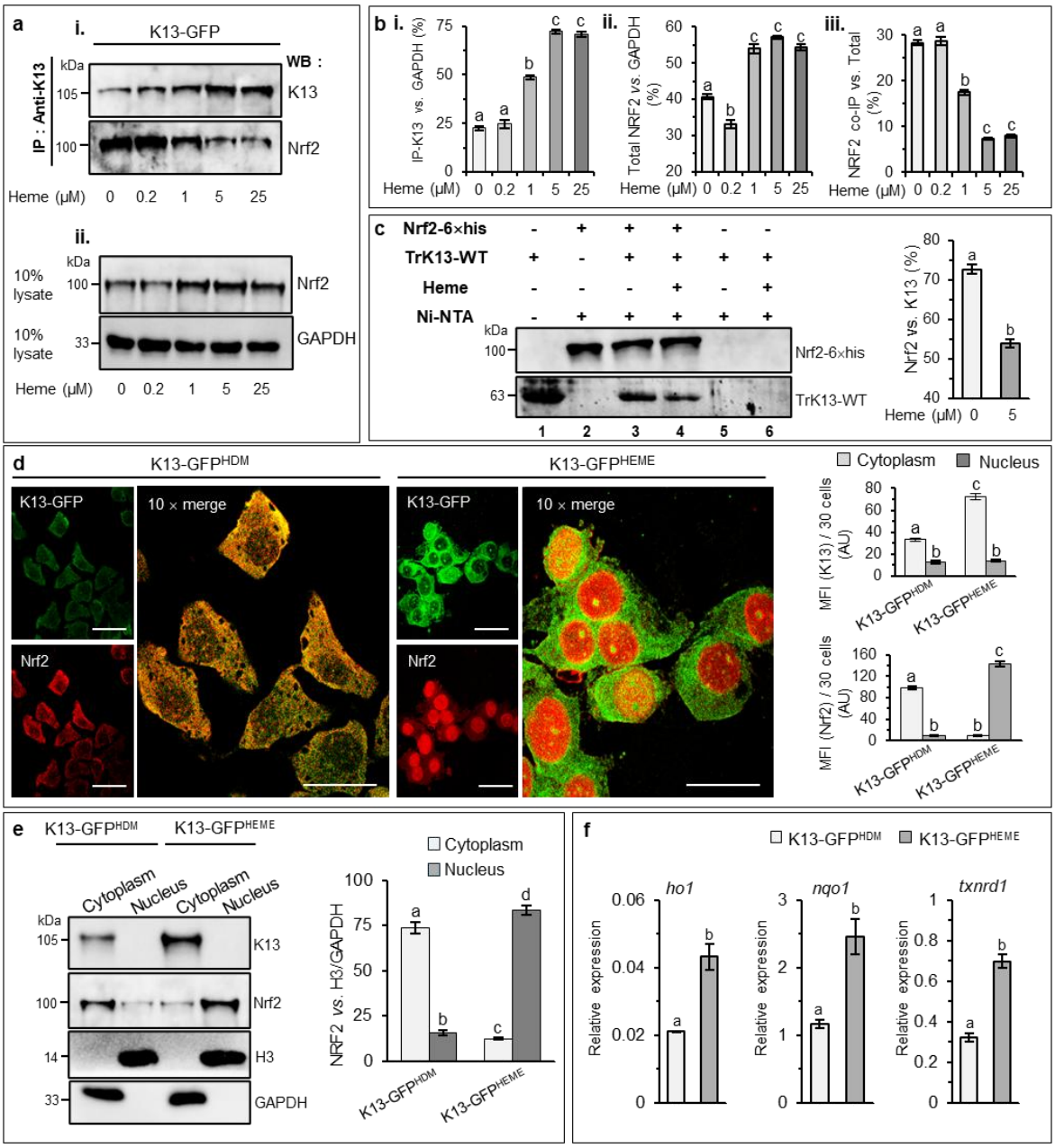

671

672 **Fig. 2. Heme alters the level and dynamics of the redox reporter Nrf2 in K13-GFP-expressing**
673 **cells. a. i.** Western blots showing immunoprecipitated K13-GFP (top) and the co-associated Nrf2
674 (bottom) protein from K13-GFP cells cultured in HDM or in the presence of different concentrations of
675 heme. **ii.** Total Nrf2 (top) and GAPDH (bottom, as loading control) in the cellular lysates for conditions
676 in a. **b.** Graphical densitometric analyses of K13-GFP, total Nrf2 and co-purified Nrf2 for data shown
677 in a. **c.** Western blots (left) and graphical densitometric analysis (right) showing reduced co-
678 purification of the heme-bound (lane 4) recombinant K13 (TrK13-WT) by the recombinant Nrf2-6×his

679 protein (pre-bound to Ni-NTA beads) as compared to the heme-free TrK13-WT protein (lane 3) .
680 Lanes 1 and 2 indicate TrK13-WT input and the Ni-NTA bound Nrf2-6×his protein, respectively. Lanes
681 5 and 6 show no nonspecific binding of heme-free or heme-bound TrK13-WT protein to the Ni-NTA
682 beads, respectively. **d.** IFA images showing increased levels of K13-GFP (green) fluorescence and
683 nuclear localization of Nrf2 (red; right panel) in the K13-GFP^{HEME} cells (right). In K13-GFP^{HDM} cells
684 (right), the Nrf2 fluorescence distribution was predominantly cytoplasmic. Scale bar, 5 μm. **e.**
685 Western blots and graphical densitometric quantitation for cytoplasmic and nuclear fractionation of
686 Nrf2 in K13-GFP^{HDM} and K13-GFP^{HEME} cells. **f.** RT-qPCR data showing relative expression of stress-
687 response genes in K13-GFP^{HDM} cells and K13-GFP^{HEME} cells. Molecular weights (in kDa) are as
688 indicated. Error bars represent mean of three technical replicates ± SE. Statistical significance was
689 calculated by one-way Anova. Distinct alphabets represent significant difference at p.adj ≤ 0.05.

Fig. 3

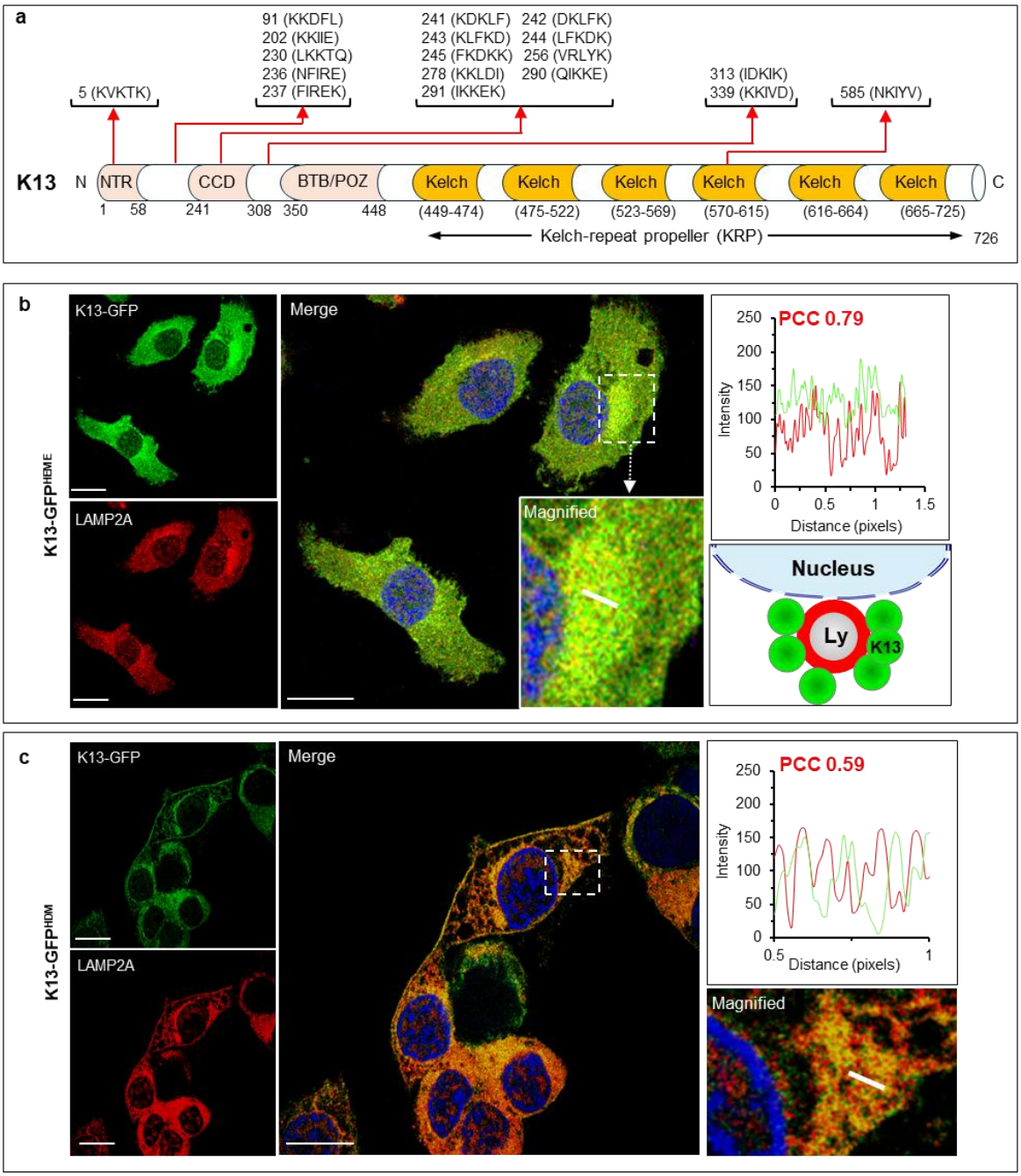

Fig. 3. Signature motifs of autophagy in K13 and heme-dependent co-association with LAMP2A. a. Schematic showing the distribution of 18 putative KFERQ-like motifs in different domains of K13, as identified by KFERQ finder v0.8 (*https://rshine.einsteinmed.edu*). NTR, N-terminus domain; CCD, coiled-coil domain; BTB-POZ, Broad-complex, tramtrack and bric-a-brac (BTB)-poxvirus and zinc-finger (POZ) domain. **b-c.** IFA images (left) and RGB intensity plots (right) showing the extent of colocalization between K13-GFP (green) and LAMP2A (red) in K13-GFP^{HDM} (b) and K13-GFP^{HEME}

697 cells (c). Pearson's correlation coefficient (PCC) values for the selected region (white bar) are
698 indicated in red text. Magnified images of the white-dotted boxed region for respective cells are also
699 shown. Schematic in b represents proposed association of K13 with lysosomes based on the inset
700 magnification. Scale bar, 5 μm is shown at the bottom of each image. Cell nucleus (blue) stained with
701 Hoechst 33342.

702

703

Fig. 4

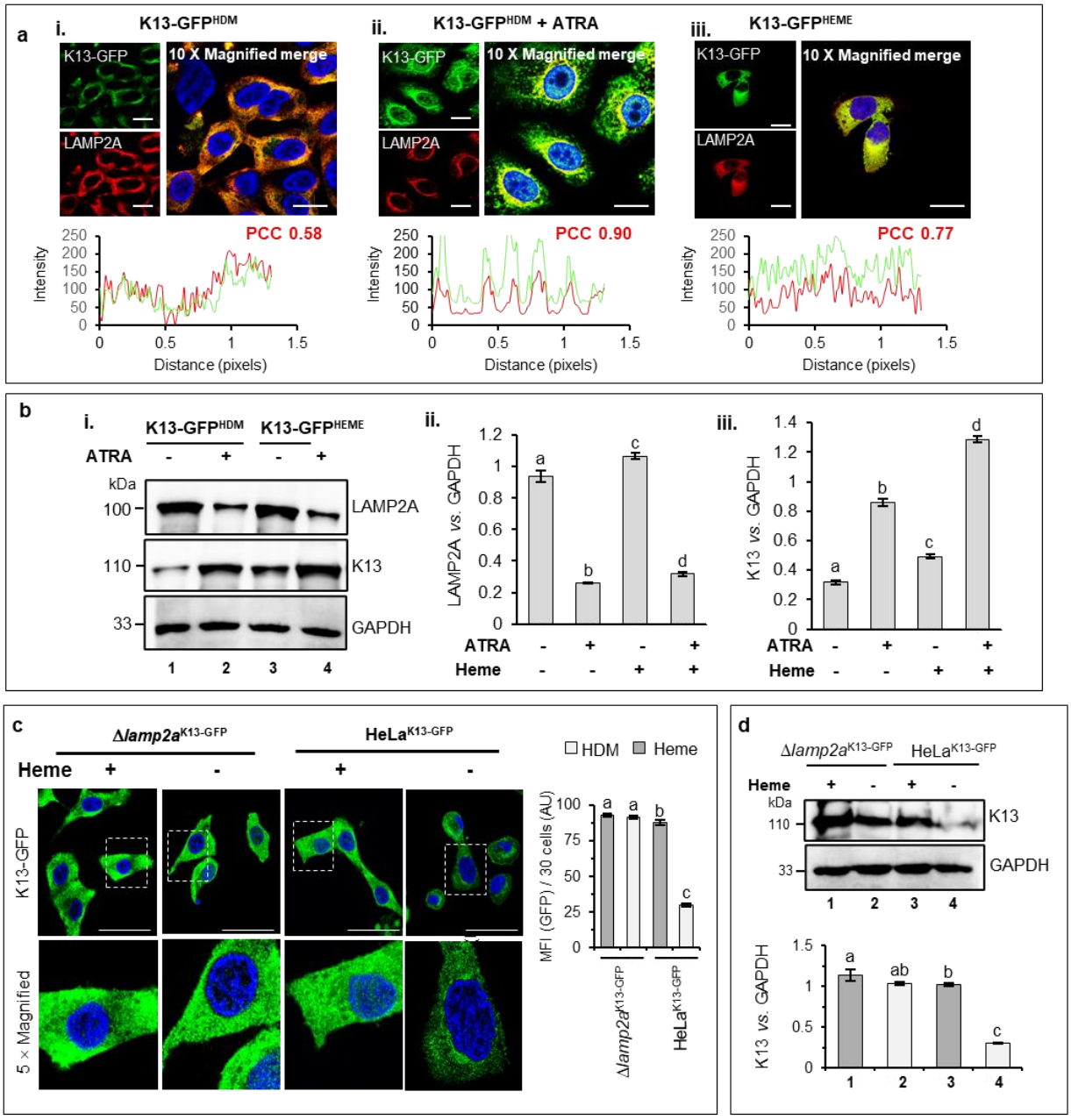

704

705 **Fig. 4. Reduction or knockout of LAMP2A decreases degradation of K13-GFP under HDM**
706 **conditions. a.** In Du145 cells, IFA images and RGB intensity plots (with PCC values) showing relative
707 colocalization between K13-GFP (green) and LAMP2A (red) in K13-GFP^{HDM} cells in the absence (i) or
708 presence (ii) of ATRA (inhibitor of LAMP2A expression) compared to K13-GFP^{HEME} cells (iii).
709 Corresponding fluorescence and merged images were acquired under identical optics and exposure

710 conditions. **b.** Western blots (i) and fold change (ii-iii) for LAMP2A (top), K13-GFP (middle) in the
711 absence or presence of ATRA in cells expressing K13-GFP^{HDM} (lanes 1-2) or K13-GFP^{HEME} (lanes 3-
712 4). GAPDH (bottom) was the loading control. **c.** In HeLa cells, IFA images (left), and graphical MFI
713 (right) of K13-GFP fluorescence (green) in transgenic *Δlamp2a*$^{K13\text{-}GFP}$ and parental HeLa$^{K13\text{-}GFP}$ cells
714 under HDM (-) or heme-supplemented (+) conditions. **d.** Western blots (top) and graphical fold
715 change of K13-GFP (top) in transgenic *Δlamp2a*$^{K13\text{-}GFP}$ (lanes 1-2) and parental HeLa (lanes 3-4) cells
716 under HDM (lanes 2 and 4) or heme-supplemented (lanes 1 and 3) conditions. GAPDH was the
717 loading control. Scale bar for IFA images, 5 μm. Boxed (white dotted) images are magnified in sub-
718 panel. For all statistical analyses, each bar denotes the mean from three technical replicates ± SE.
719 Statistical significance was calculated by one-way Anova. Distinct alphabets represent difference at
720 p.adj ≤ 0.05. Molecular weights (in kDa) for all blots are as indicated.

Fig. 5

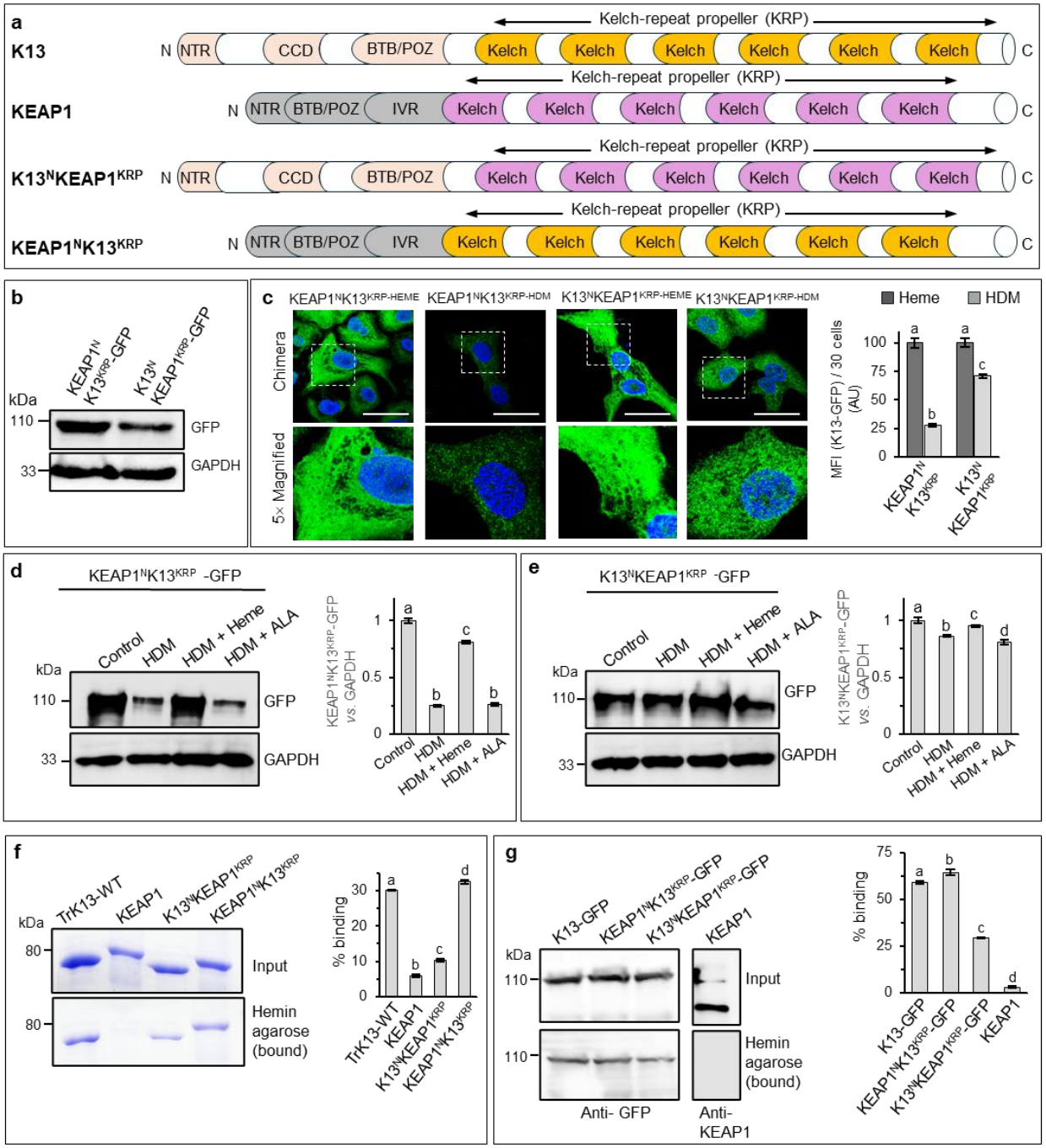

721

722 **Fig. 5. The K13 KRP domain confers heme-dependent stability and heme-binding**
723 **characteristics to KEAP1. a.** Schematics for domain organization in K13, KEAP1, K13^{N}KEAP1^{KRP}
724 and KEAP1^{N}K13^{KRP} chimeric proteins. NTR, N-terminus domain; CCD, coiled-coil domain; BTB-POZ,
725 Broad-complex, tramtrack and bric-a-brac (BTB)-poxvirus and zinc-finger (POZ) domain; IVR,
726 intervening region. **b.** Western blot detecting K13^{N}KEAP1^{KRP}-GFP and KEAP1^{N}K13^{KRP}-GFP
727 (arrowhead) chimeras in transgenic Du145 cells. Loading control is GAPDH. **c.** IFA images and mean

728 fluorescence intensity (MFI) of $K13^{N}KEAP1^{KRP}$-GFP and $KEAP1^{N}K13^{KRP}$-GFP cells cultured under
729 HDM or heme-repleted conditions. Nuclei stained with Hoechst 33342 (blue), scale bar, 5 µm.
730 Respective boxed (white dotted) regions are magnified and shown below. **d-e.** Western blots (left)
731 and densitometric fold change (right) in $KEAP1^{N}K13^{KRP}$-GFP (d) and $K13^{N}KEAP1^{KRP}$ (e) protein band
732 intensities under HDM, heme-repleted or heme precursor aminolevulinic acid (ALA)-containing HDM
733 conditions. **f-g.** Coomassie-stained SDS-PAGE (f) and western blots (g) showing hemin agarose
734 binding by indicated KEAP1-K13 recombinant proteins or chimeras (f) or from respective transgenic
735 Du145 cellular lysates (g). Percentage binding (as compared to the total input) is shown graphically.
736 Molecular weights (in kDa) for SDS-PAGE and western blots are as indicated. Error bars in the
737 graphs represent mean of three technical replicates ± SE. Statistical significance was calculated by
738 one-way Anova. Distinct alphabets represent significant difference at p.adj ≤ 0.05.

Fig. 6

a i.

Transgenic Du145 cell line	IC_{50} (μM)		% change in IC_{50}
	HDM	HEME (5 μM)	
GFP	117.7 ± 0.9	114.7 ± 0.5	2.6 ± 0.7 %
K13-GFP	109.7 ± 0.2	93.8 ± 0.4	18.2 ± 0.6 %
KEAP1	87.8 ± 0.2	83.9 ± 0.8	6.1 ± 1.4 %
$KEAP1^{N}K13^{KRP}$-GFP	102.3 ± 0.3	84.8 ± 0.9	23.7 ± 1.4 %
$K13^{N}KEAP1^{KRP}$-GFP	80.8 ± 0.1	73.9 ± 0.9	13.5 ± 1.8 %

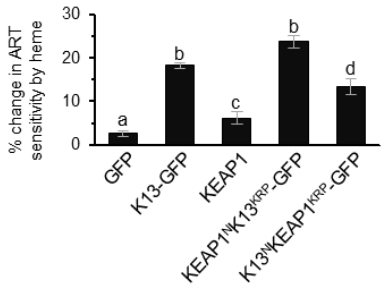

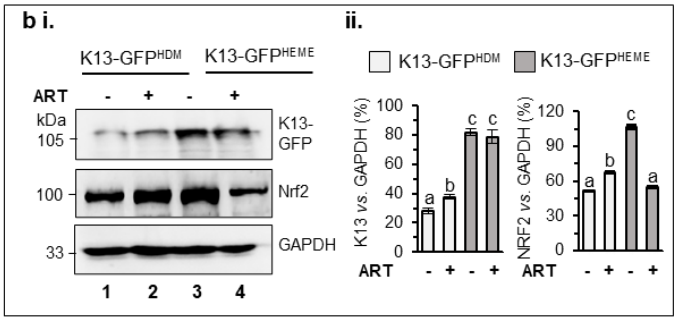

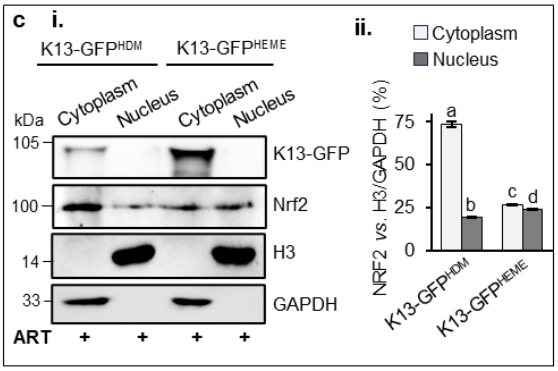

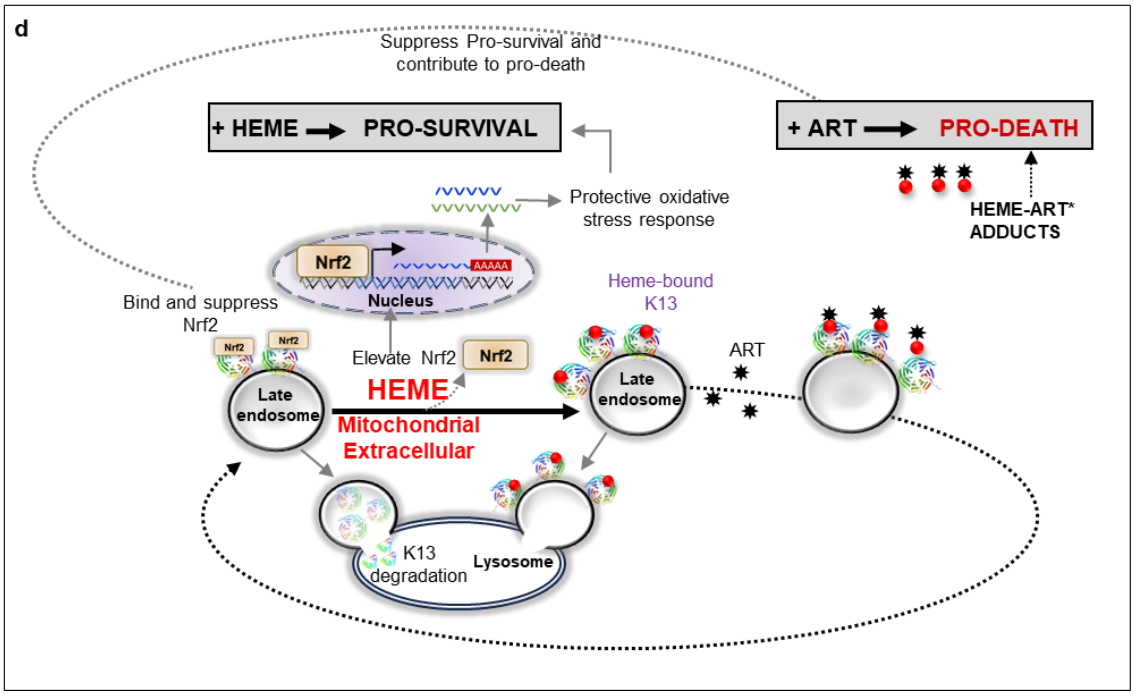

739

740 **Fig. 6. Dynamics of K13, heme and Nrf2 in a redox survival mechanism that promotes ART-**
741 **induced death. a.** IC_{50} values (μM, i) and change in percentage sensitivity to ART (right, ii) in
742 respective transgenic Du145 cell lines on supplementation with 5 μM heme. **b.** Western blots (i) and
743 quantitative densitometric analysis (versus GAPDH, ii) for K13-GFP (top) and Nrf2 (middle) in K13-

744 GFP^{HDM} (lanes 1 and 2) and K13-GFP^{HEME} (lanes 3 and 4) cells in the absence (lanes 1 and 3) or
745 presence (lanes 2 and 4) of ART. GAPDH (bottom) is the loading control. **c.** Western blots (i) and
746 graphical densitometric quantitation (ii) for cytoplasmic and nuclear fractionation of K13-GFP and Nrf2
747 in K13-GFP^{HDM} and K13-GFP^{HEME} cells in the presence of ART. Molecular weight (in kDa) are as
748 indicated. Error bars in a-c represent mean of three technical replicates ± SE. Statistical significance
749 was calculated by one-way Anova. Distinct alphabets represent significant difference at p.adj ≤ 0.05.
750 **d.** Model for a redox survival mechanism that promotes artemisinin-induced death**.** Dynamics of Nrf2
751 binding by free K13, its displacement by heme inducing (i) a redox survival response and (ii) K13-
752 heme mediated activation of ART inducing oxidative pro-death response in Du145 cells.

753

754

Fig. 7

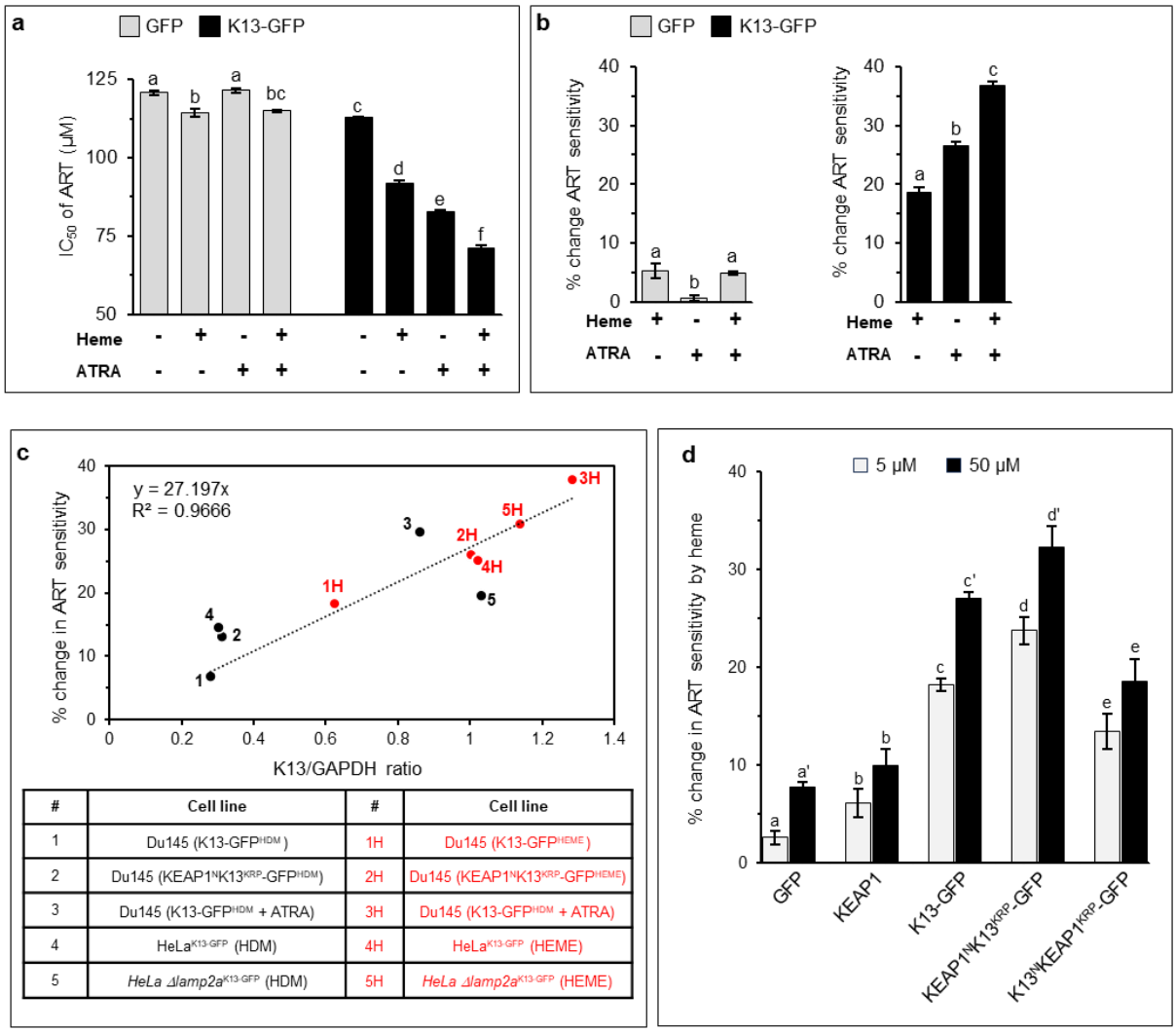

#	Cell line	#	Cell line
1	Du145 (K13-GFP^{HDM})	1H	Du145 (K13-GFP^{HEME})
2	Du145 (KEAP1^{N}K13^{KRP}-GFP^{HDM})	2H	Du145 (KEAP1^{N}K13^{KRP}-GFP^{HEME})
3	Du145 (K13-GFP^{HDM} + ATRA)	3H	Du145 (K13-GFP^{HDM} + ATRA)
4	HeLa$^{K13-GFP}$ (HDM)	4H	HeLa$^{K13-GFP}$ (HEME)
5	*HeLa Δlamp2a*$^{K13-GFP}$ (HDM)	5H	*HeLa Δlamp2a*$^{K13-GFP}$ (HEME)

755

756 **Fig. 7. ART sensitivity is increased proportional to K13 intensity. a.** IC_{50} values (μM) for GFP and
757 K13-GFP cells in presence or absence of ATRA or heme (5 μM). **b.** Effect of heme (5 μM) and ATRA
758 on percentage change in ART sensitivity in cells expressing GFP (grey bars) or K13-GFP (black
759 bars). **c.** Graph showing the percentage change in ART sensitivity as a function of K13/GAPDH
760 intensity ratio under HDM (solid black circles) or 5 μM heme-repleted (solid red circles) conditions in
761 transgenic Du145 and HeLa cells. Black dotted trendline and R-squared values are indicated.
762 Description of cells is shown at the bottom. Numbers only and numbers followed by initial 'H' indicate
763 cells cultured under HDM or 5 μM heme-repleted conditions, respectively. **d.** Graph showing change
764 in percentage sensitivity to ART at extracellular 5 μM (grey) and 50 μM (black) heme in the repleted

media. Error bars in a, b and d represent mean of three technical replicates ± SE. Statistical significance was calculated by one-way Anova. Distinct alphabets represent significant difference at p.adj ≤ 0.05.

769

Fig. 8

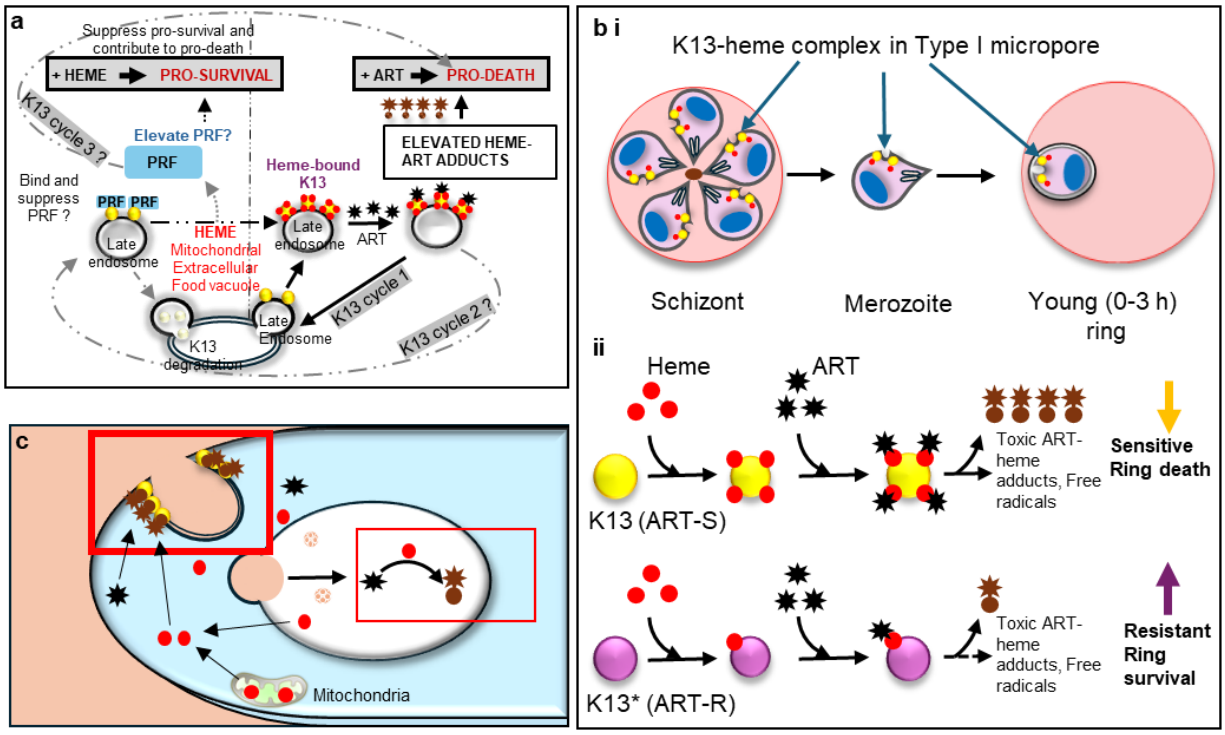

770

771 **Fig. 8. A new model for clinical ART-R, implicated by K13-heme redox survival responses and**
772 **ART-induced death. a-b.** ART induced pro-death mechanisms and their modulation in rings. Our
773 primary conclusion is for **K13 in cycle 1** (bold lines, **a**), where K13 (solid yellow circle) binds heme
774 (solid red circles, **a**) and becomes stabilized at cytoplasmic face of endosomal Type I micropore
775 membranes of merozoites and rings (shown in panel **b**). For merozoites and rings, heme may come
776 from mitochondrial and extracellular sources. K13-heme activates ART (solid black stars) to heme-
777 ART adducts (dark brown hybrid star-circles), which dissociate from K13 (resulting in suppression of
778 K13 redox sensing). Widespread toxicity of heme-ART adducts to cellular targets, triggers a pro-death
779 response in the parasite. Heme-free K13 may re-cycle back to resume heme binding and re-initiate
780 cycle 1 and reinforce death outcomes. **K13 cycle 2** may be initiated if a (yet hypothetical) parasite
781 redox factor (PRF; solid blue rectangle) binds K13 and becomes suppressed until heme-binding
782 dislodges the PRF to activate ART and pro-death effects, acting additively with cycle 1. **K13 cycle 3**
783 may be initiated upon K13 displacement of PRF to trigger pro-survival responses and reduce pro-
784 death effects of cycles 1 and 2**. b i**. Model proposing K13-heme complexes (solid yellow circles with

785 solid red circles) assemble at Type I micropores of *P. falciparum* merozoites as they develop in
786 schizonts. Released merozoites invade new red blood cells to form rings associated with Type I
787 micropores and K13-heme complexes[71]. **b ii.** In wild type rings, K13-heme trigger ART (solid black
788 stars)-induced oxidative damage radicals that destroy essential Type I micropores, resulting in ring-
789 death. K13 ART-R mutants (solid purple circles) show reduced heme binding, oxidative damage
790 enabling ring survival and ART-R. **c.** K13-heme is also catalytic for ART activation in trophozoites.
791 K13 (solid yellow circles) concentrates at cytostome structures that enable hemoglobin digestion and
792 liberation of free heme (solid red circles) in the food vacuole. Existing models propose that free heme
793 activates ART (solid black stars) to toxic heme-ART adducts (dark brown hybrid star-circle) in the food
794 vacuole (see red box). We propose that heme from the food vacuole and other sources (like the
795 mitochondria) transported to the parasite bind K13 concentrated at the cytostome, which greatly
796 stimulates formation of activated ART, and toxic heme-ART adducts (dark brown hybrid star-circle in
797 bold red box) compared to encounters of ART with free heme in the food vacuole, thus explaining why
798 K13 mutants do not confer ART-R at these stages.

799

800 **References**

801 1. Nosten, F. & White, N. J. Artemisinin-based combination treatment of falciparum malaria. *Am.*
802 *J. Trop. Med. Hyg.* **77**, 181–192 (2007).

803 2. Eastman, R. T. & Fidock, D. A. Artemisinin-based combination therapies: A vital tool in efforts
804 to eliminate malaria. *Nature Reviews Microbiology* vol. 7 (2009).

805 3. Pires, C. V. *et al.* Oxidative stress changes the effectiveness of artemisinin in Plasmodium
806 falciparum. *MBio* **15**, (2024).

807 4. Zhu, P. & Zhou, B. The Antagonizing Role of Heme in the Antimalarial Function of Artemisinin:
808 Elevating Intracellular Free Heme Negatively Impacts Artemisinin Activity in Plasmodium
809 falciparum. *Molecules* **27**, (2022).

810 5. Rocamora, F. *et al.* Oxidative stress and protein damage responses mediate artemisinin
811 resistance in malaria parasites. *PLoS Pathog* **14**, e1006930 (2018).

812 6. Ariey, F. *et al.* A molecular marker of artemisinin-resistant Plasmodium falciparum malaria.
813 *Nature* **505**, 50–55 (2014).

814 7. Straimer, J. *et al.* Drug resistance. K13-propeller mutations confer artemisinin resistance in
815 Plasmodium falciparum clinical isolates. *Science (80-.).* **347**, 428–431 (2015).

816 8. WHO. World malaria report 2024. https://www.who.int/teams/global-malaria-
817 programme/reports/world-malaria-report-2024 (2024).

818 9. Cui, L., Mharakurwa, S., Ndiaye, D., Rathod, P. K. & Rosenthal, P. J. Antimalarial drug
819 resistance: Literature review and activities and findings of the ICEMR network. *American*
820 *Journal of Tropical Medicine and Hygiene* vol. 93 (2015).

821 10. Menard, D. *et al.* A Worldwide Map of Plasmodium falciparum K13-Propeller Polymorphisms.
822 *N Engl J Med* **374**, 2453–2464 (2016).

823 11. Xie, S. C., Ralph, S. A. & Tilley, L. K13, the Cytostome, and Artemisinin Resistance. *Trends in*
824 *Parasitology* vol. 36 (2020).

825 12. Blasco, B., Leroy, Di. & Fidock, D. A. Antimalarial drug resistance: Linking Plasmodium
826 falciparum parasite biology to the clinic. *Nature Medicine* vol. 23 (2017).

827 13. Fairhurst, R. M. & Dondorp, A. M. Artemisinin-Resistant Plasmodium falciparum Malaria.
828 *Microbiol Spectr* **4**, (2016).

829 14. Bhattacharjee, S. *et al.* Remodeling of the malaria parasite and host human red cell by vesicle
830 amplification that induces artemisinin resistance. *Blood* **131**, 1234–1247 (2018).

831 15. Birnbaum, J. *et al.* A Kelch13-defined endocytosis pathway mediates artemisinin resistance in
832 malaria parasites. *Science (80-.).* **367**, 51–59 (2020).

833 16. Tutor, M. V. *et al.* The Plasmodium falciparum artemisinin resistance-associated protein Kelch
834 13 is required for formation of normal cytostomes. *bioRxiv* (2023).

835 17. Meshnick, S. R. Artemisinin: Mechanisms of action, resistance and toxicity. in *International*
836 *Journal for Parasitology* vol. 32 (2002).

837 18. Sutherland, C. J., Henrici, R. C. & Artavanis-Tsakonas, K. Artemisinin susceptibility in the
838 malaria parasite Plasmodium falciparum: propellers, adaptor proteins and the need for cellular
839 healing. *FEMS Microbiol. Rev.* **45**, (2021).

840 19. Ribbiso, K. A. *et al.* Artemisinin-based drugs target the plasmodium falciparum heme
841 detoxification pathway. *Antimicrob. Agents Chemother.* **65**, (2021).

842 20. Zhang, S. & Gerhard, G. S. Heme activates artemisinin more efficiently than hemin, inorganic
843 iron, or hemoglobin. *Bioorganic Med. Chem.* **16**, (2008).

844 21. Rosenthal, M. R. & Ng, C. L. Plasmodium falciparum Artemisinin Resistance: The Effect of
845 Heme, Protein Damage, and Parasite Cell Stress Response. *ACS Infectious Diseases* vol. 6
846 (2020).

847 22. Yu, X. *et al.* Ring-stage growth arrest: Metabolic basis of artemisinin tolerance in Plasmodium
848 falciparum. *iScience* **26**, (2023).

849 23. Platon, L. & Ménard, D. Plasmodium falciparum ring-stage plasticity and drug resistance.
850 *Trends in Parasitology* vol. 40 (2024).

851 24. Rahman Abdur *et al.* Artemisinin-resistant Plasmodium falciparum Kelch13 mutant proteins
852 display reduced heme-binding affinity and decreased artemisinin activation. *Commun Biol.* **13**,
853 1499 (2024).

854 25. Severance, S. & Hamza, I. Trafficking of heme and porphyrins in metazoa. *Chem. Rev.* **109**,
855 (2009).

856 26. Schultz, I. J., Chen, C., Paw, B. H. & Hamza, I. Iron and porphyrin trafficking in heme
857 biogenesis. *Journal of Biological Chemistry* vol. 285 (2010).

858 27. Ascenzi, P. *et al.* Hemoglobin and heme scavenging. *IUBMB Life* vol. 57 (2005).

859 28. Morgan, W. T., Heng Liem, H., Sutor, R. P. & Muller-Eberhard, U. Transfer of heme from
860 heme-albumin to hemopexin. *BBA - Gen. Subj.* **444**, (1976).

861 29. Yi, L. & Ragsdale, S. W. Evidence that the heme regulatory motifs in heme oxygenase-2 serve

862 as a thiol/disulfide redox switch regulating heme binding. *J. Biol. Chem.* **282**, (2007).

863 30. Gamiz-Arco, G. *et al.* Heme-binding enables allosteric modulation in an ancient TIM-barrel
864 glycosidase. *Nat. Commun.* **12**, (2021).

865 31. Chiabrando, D., Vinchi, F., Fiorito, V., Mercurio, S. & Tolosano, E. Heme in pathophysiology: A
866 matter of scavenging, metabolism and trafficking across cell membranes. *Front. Pharmacol.* **5**,
867 (2014).

868 32. Jiang Tempel W. Loppnau P. Graslund S. He H. Ravichandran M. Seitova A. Arrowsmith C.H.
869 Edwards A.M. Bountra C. El Bakkouri M. Senisterra G. Osman K.T. Lovato D.V. Hui R.
870 Hutchinson A. Lin Y.H., D. Q. Crystal Structure Analysis of Kelch protein from Plasmodium
871 falciparum. *Struct. Genomics Consort.* (2015).

872 33. Li, X., Zhang, D., Hannink, M. & Beamer, L. J. Crystal structure of the Kelch domain of human
873 Keap1. *J. Biol. Chem.* **279**, 54750–54758 (2004).

874 34. Billett, H. H. *Hemoglobin and Hematocrit*. *Clinical Methods: The History, Physical, and*
875 *Laboratory Examinations* (Butterworths, 1990).

876 35. Aich, A., Freundlich, M. & Vekilov, P. G. The free heme concentration in healthy human
877 erythrocytes. *Blood Cells, Mol. Dis.* **55**, (2015).

878 36. Donegan, R. K., Moore, C. M., Hanna, D. A. & Reddi, A. R. Handling heme: The mechanisms
879 underlying the movement of heme within and between cells. *Free Radical Biology and*
880 *Medicine* vol. 133 (2019).

881 37. White, N. J. Anaemia and malaria. *Malaria Journal* vol. 17 (2018).

882 38. Nagaraj, V. A. *et al.* Malaria Parasite-Synthesized Heme Is Essential in the Mosquito and Liver
883 Stages and Complements Host Heme in the Blood Stages of Infection. *PLoS Pathog.* **9**,
884 (2013).

885 39. Ke, H. *et al.* The heme biosynthesis pathway is essential for Plasmodium falciparum
886 development in mosquito stage but not in blood stages. *J. Biol. Chem.* **289**, (2014).

887 40. Abshire, J. R., Rowlands, C. J., Ganesan, S. M., So, P. T. C. & Niles, J. C. Quantification of
888 labile heme in live malaria parasites using a genetically encoded biosensor. *Proc. Natl. Acad.*
889 *Sci. U. S. A.* **114**, (2017).

890 41. Heller, L. E. & Roepe, P. D. Quantification of Free Ferriprotoporphyrin IX Heme and Hemozoin
891 for Artemisinin Sensitive versus Delayed Clearance Phenotype Plasmodium falciparum
892 Malarial Parasites. *Biochemistry* **57**, (2018).

893 42. Stone, K. R., Mickey, D. D., Wunderli, H., Mickey, G. H. & Paulson, D. F. Isolation of a human
894 prostate carcinoma cell line (DU 145). *Int. J. Cancer* **21**, (1978).

895 43. Jayakumar, S., Kunwar, A., Sandur, S. K., Pandey, B. N. & Chaubey, R. C. Differential
896 response of DU145 and PC3 prostate cancer cells to ionizing radiation: Role of reactive
897 oxygen species, GSH and Nrf2 in radiosensitivity. *Biochim. Biophys. Acta - Gen. Subj.* **1840**,
898 (2014).

899 44. Zhang, P. *et al.* Loss of Kelch-like ECH-associated protein 1 function in prostate cancer cells
900 causes chemoresistance and radioresistance and promotes tumor growth. *Mol Cancer Ther* **9**,
901 336–346 (2010).

902 45. Morgan, W. T. & Smith, A. Domain structure of rabbit hemopexin. Isolation and
903 characterization of a heme-binding glycopeptide. *J. Biol. Chem.* **259**, (1984).

904 46. Tolosano, E. & Altruda, F. Hemopexin: Structure, function, and regulation. *DNA and Cell*
905 *Biology* vol. 21 (2002).

906 47. Goel, N. *et al.* Plasmodium falciparum Kelch13 and its artemisinin-resistant mutants assemble
907 as hexamers in solution: a SAXS data-driven modelling study. *FEBS J.* **289**, (2022).

908 48. Makarska-Bialokoz, M. Interactions of hemin with bovine serum albumin and human
909 hemoglobin: A fluorescence quenching study. *Spectrochim. Acta - Part A Mol. Biomol.*
910 *Spectrosc.* **193**, (2018).

911 49. Kensler, T. W., Wakabayashi, N. & Biswal, S. Cell survival responses to environmental
912 stresses via the Keap1-Nrf2-ARE pathway. *Annual Review of Pharmacology and Toxicology*

913 vol. 47 (2007).

914 50. Mense, S. M. & Zhang, L. Heme: A versatile signaling molecule controlling the activities of
915 diverse regulators ranging from transcription factors to MAP kinases. *Cell Research* vol. 16
916 (2006).

917 51. Taguchi, K. *et al.* Keap1 degradation by autophagy for the maintenance of redox homeostasis.
918 *Proc. Natl. Acad. Sci. U. S. A.* **109**, (2012).

919 52. Kirchner, P. *et al.* Proteome-wide analysis of chaperone-mediated autophagy targeting motifs.
920 *PLoS Biol.* **17**, (2019).

921 53. Agarraberes, F. A. & Dice, J. F. A molecular chaperone complex at the lysosomal membrane
922 is required for protein translocation. *J. Cell Sci.* **114**, (2001).

923 54. Stricher, F., Macri, C., Ruff, M. & Muller, S. HSPA8/HSC70 chaperone protein. *Autophagy* **9**,
924 (2013).

925 55. Ikami, Y., Terasawa, K., Watabe, T., Yokoyama, S. & Hara-Yokoyama, M. The two-domain
926 architecture of LAMP2A within the lysosomal lumen regulates its interaction with
927 HSPA8/Hsc70. *Autophagy Reports* vol. 1 (2022).

928 56. Zhu, L. *et al.* Chaperone-mediated autophagy degrades Keap1 and promotes Nrf2-mediated
929 antioxidative response. *Aging Cell* **21**, (2022).

930 57. Anguiano, J. *et al.* Chemical modulation of chaperone-mediated autophagy by retinoic acid
931 derivatives. *Nat. Chem. Biol.* **9**, (2013).

932 58. Probst, B. L., McCauley, L., Trevino, I., Wigley, W. C. & Ferguson, D. A. Cancer cell growth is
933 differentially affected by constitutive activation of NRF2 by KEAP1 deletion and
934 pharmacological activation of NRF2 by the synthetic triterpenoid, RTA 405. *PLoS One* **10**,
935 (2015).

936 59. Gnadig, N. F. *et al.* Insights into the intracellular localization, protein associations and
937 artemisinin resistance properties of Plasmodium falciparum K13. *PLoS Pathog* **16**, e1008482

938 (2020).

939 60. Siddiqui, G., Srivastava, A., Russell, A. S. & Creek, D. J. Multi-omics Based Identification of
940 Specific Biochemical Changes Associated With PfKelch13-Mutant Artemisinin-Resistant
941 Plasmodium falciparum. *J Infect Dis* **215**, 1435–1444 (2017).

942 61. Atul *et al.* Artemisinin resistance in P. falciparum: Probing the interacting partners of Kelch13
943 protein in parasite. *J. Glob. Antimicrob. Resist.* (2023) doi:10.1016/j.jgar.2023.08.012.

944 62. Müller, S. Redox and antioxidant systems of the malaria parasite Plasmodium falciparum.
945 *Molecular Microbiology* vol. 53 (2004).

946 63. Hott, A. *et al.* Artemisinin-resistant Plasmodium falciparum parasites exhibit altered patterns of
947 development in infected erythrocytes. *Antimicrob Agents Chemother* **59**, 3156–3167 (2015).

948 64. Witkowski, B. *et al.* Novel phenotypic assays for the detection of artemisinin-resistant
949 Plasmodium falciparum malaria in Cambodia: in-vitro and ex-vivo drug-response studies.
950 *Lancet Infect Dis* **13**, 1043–1049 (2013).

951 65. Birnbaum, J. *et al.* A genetic system to study Plasmodium falciparum protein function. *Nat*
952 *Methods* **14**, 450–456 (2017).

953 66. Mbengue, A. *et al.* A molecular mechanism of artemisinin resistance in Plasmodium falciparum
954 malaria. *Nature* **520**, 683–687 (2015).

955 67. Wan, W. *et al.* The Toxoplasma micropore mediates endocytosis for selective nutrient salvage
956 from host cell compartments. *Nat. Commun.* **14**, (2023).

957 68. Koreny, L. *et al.* Stable endocytic structures navigate the complex pellicle of apicomplexan
958 parasites. *Nat. Commun.* **14**, (2023).

959 69. Garnham, P. C. C., Bird, R. G. & Baker, J. R. Electron microscope studies of motile stages of
960 malaria parasites: III. The ookinetes of Haemamoeba and Plasmodium. *Trans. R. Soc. Trop.*
961 *Med. Hyg.* **56**, 116–120 (1962).

962 70. Jiong Yang , Shaojun Long , Geoff Hide , Zhao-Rong Lun, D.-H. L. Apicomplexa micropore:

963 history, function, and formation. *Trends Parasitol.* **40**, 416–426 (2024).

964 71. Haldar, K. & Bhattacharjee, S. Vesicular mechanisms of drug resistance in apicomplexan
965 parasites. *Microbiol. Mol. Biol. Rev.* **89**, 1–17 (2025).

966 72. Wang, J. *et al.* Haem-activated promiscuous targeting of artemisinin in Plasmodium
967 falciparum. *Nat Commun* **6**, 10111 (2015).

968 73. Gao, P. *et al.* Profiling the Antimalarial Mechanism of Artemisinin by Identifying Crucial Target
969 Proteins. *Engineering* (2023) doi:10.1016/j.eng.2023.06.001.

970 74. Sinai, A. P. & Roepe, P. D. Autophagy in Apicomplexa: a life sustaining death mechanism?
971 *Trends Parasitol* **28**, 358–364 (2012).

972 75. Ghosh, D., Walton, J. L., Roepe, P. D. & Sinai, A. P. Autophagy is a cell death mechanism in
973 Toxoplasma gondii. *Cell. Microbiol.* **14**, (2012).

974 76. Suzuki, K., Bose, P., Leong-Quong, R. Y., Fujita, D. J. & Riabowol, K. REAP: A two minute cell
975 fractionation method. *BMC Res. Notes* **3**, (2010).

976